# Chapter 2
# Characterization of Pre-bond Contamination and Aging Effects for CFRP Bonded Joints Using Reference Laboratory Methods, Mechanical Tests, and Numerical Simulation


**Konstantinos Tserpes, Elli Moutsompegka, Mareike Schlag, Kai Brune, Christian Tornow, Ana Reguero Simón, and Romain Ecault**

**Abstract** In this chapter, the pre-bond contamination and ageing effects on carbon fiber reinforced plastic (CFRP) adherends and CFRP bonded joints are characterized by means of reference laboratory non-destructive testing (NDT) methods, mechanical tests, and numerical simulation. Contaminations from two fields of application are considered, namely in aircraft manufacturing (i.e. production) and for in-service bonded repair. The production-related scenarios comprise release agent, moisture, and fingerprint, while the repair-related scenarios comprise fingerprint, thermal degradation, de-icing fluid, and a faulty curing of the adhesive. For each scenario, three different levels of contamination were pre-set and applied, namely low, medium and high level. Furthermore, two types of samples were tested, namely coupons and pilot samples (a stiffened panel and scarf repairs). The CFRP adherends were contaminated prior to bonding and the obtained surfaces were characterized using X-ray photoelectron spectroscopy. After bonding, the joints were tested by ultrasonic testing. To characterize the effects of each contamination on the strength of the bonded joints, mode-I and mode-II fracture toughness tests, and novel centrifuge tests were conducted on the coupons, while tensile tests were performed on the scarfed samples. Additionally, numerical simulation was performed on CFRP stiffened panels under compression using the LS-DYNA finite element (FE) platform.

K. Tserpes (✉) · E. Moutsompegka
Laboratory of Technology & Strength of Materials, Department of Mechanical Engineering & Aeronautics, University of Patras, 26500 Patras, Greece
e-mail: kitserpes@upatras.gr

M. Schlag · K. Brune · C. Tornow
Fraunhofer Institute for Manufacturing Technology and Advanced Materials IFAM, Wiener Str. 12, 28359 Bremen, Germany

A. Reguero Simón
Aernnova Composites Illescas Sau, Parque Industrial y Tecnológico, Avda Barajas, 3 Illescas, 45200 Toledo, Spain

R. Ecault
Airbus Operations S.A.S., 316, route de Bayonne, B.P. D4101, 31060 Toulouse Cedex 9, France



W. Leite Cavalcanti et al. (eds.), *Adhesive Bonding of Aircraft Composite Structures*,
https://doi.org/10.1007/978-3-319-92810-4_2

**Keywords** Pre-bond contamination · Hygrothermal aging · Fracture toughness · Centrifuge testing · Ultrasound testing · X-ray photoelectron spectroscopy

## 2.1 Introduction

The use of adhesive bonding in aircraft structures is increasing, both in the assembly of structural parts and when applying composite patch repairs due to the numerous advantages it offers over conventional joining techniques [1–4]. These include a more uniform stress distribution in the area of the joint, the ability to join dissimilar materials, the improved fatigue properties, and the attractive strength to weight ratio. However, the use of adhesive bonding technology is presently limited to the joining and patch repairing of secondary structures that are not load-critical. Amongst the reasons inhibiting the certification of adhesive bonding for primary structures is the sensitivity of the bondline integrity to the presence of defects, which might counteract the strength of the joints. These defects are not accessible to visual monitoring during the bonding process, and they usually are caused by a pre-bond contamination of the adherend surface during either the manufacture of the joints or their repairs. As conditions on the aircraft production line and in the maintenance/overhaul shed are different, defects are categorized as either production-related or repair-related. Table 2.1 lists the pre-bond contamination scenarios under consideration in the ComBoNDT project.

Amongst the defects that might arise during the manufacture of adhesive joints, the most critical ones are those that are not detectable by the available NDT methods. In addition to developing extended NDT (ENDT) methods capable of detecting such effects [6], evaluating their effect on the strength of adhesive joints is of equal importance. Early experimental studies conducted within the ENCOMB project [1, 7, 8] have shown that undetectable defects caused by pre-bond contamination may significantly degrade the mode-I fracture toughness of CFRP joints. In the ComBoNDT project, the experimental characterization has extended the current state of research by conducting mode-I fracture toughness tests for additional contamination scenarios, mode-II tests on the complete set of contamination scenarios (Table 2.1), and novel centrifuge tests. The centrifuge tests are fast and cost-effective tests that can be used to determine the adhesion strength of bonded joints. They serve as an alternative to the fracture toughness tests, which are more expensive and time consuming. In the test program of the ComBoNDT project, mode-II tests on aged

**Table 2.1** The contamination scenarios studied in Chaps. 2 through 5 in the ComBoNDT project [5]

| Production-related (P) | Repair-related (R) |
|---|---|
| Release agent (P-RA) | Thermal degradation (R-TD) |
| Moisture (P-MO) | De-icing fluid (R-DI) |
| Fingerprint (P-FP) | Fingerprint (R-FP) |
| | Faulty curing of the adhesive (R-FC) |

joints have been also conducted with the aim of assessing the combined effect of pre-bond defects and after-bond hygrothermal aging. The material geometry tested comprises not only coupon-level samples, but also a series of samples that have more complex geometries derived from real geometries in the fields of application and are highly relevant for aerospace applications. These are the pilot samples and consist of scarfed samples and individual aerospace component parts (stiffened panels). These samples are used to evaluate the efficiency and check the applicability of ENDT methods on more complex/curved geometries with multiple contaminations in conjunction with a clean reference condition. With these samples, ENDT methods can be adapted to overcome the limitations arising from measurements on non-flat surfaces.

The debonding process is already complicated since it involves a three-material system (adherend, adhesive, and adherend/adhesive interface) as well as the geometric challenges of the parts themselves. Therefore, to determine the effects of the contaminations on the bonded joints of individual aerospace component parts, a numerical simulation was performed under compression loading using the LS-DYNA finite element (FE) platform.

The present chapter describes the respective contributions of the individual partners of the ComBoNDT consortium. The manufacturing of the CFRP adherends for the coupons and the pilot samples was performed by Aernnova Composites; the pre-bond contamination and the bonding of the samples was performed by Fraunhofer IFAM; the characterization of the adherends using X-ray photoelectron spectroscopy was performed by Fraunhofer IFAM; the ultrasound testing of the bonded plates and pilot samples was performed by Airbus; the mechanical testing of the coupons and the pilot samples as well as the aging of the coupons was performed by the University of Patras; and the numerical simulation of the stiffened panels was also conducted by the University of Patras. The datasets obtained from the mechanical testing represent design-relevant operand features. The subsequently detailed procedures offer a well-tried, step-by-step approach for compiling these features and, therefore, constitute an essential input into the framework of the applied concept for the quality assessment of adhesively bonded joints described in this book.

## 2.2 Materials and Sample Geometries

### *2.2.1 Basic Materials*

Hexcel® M21E was used for the preparation of the test coupons. HexPly M21E/IMA, developed from Hexcel®'s M21 third-generation thermosetting epoxy resin system, uses an intermediate modulus fiber to balance superior strength and stiffness, and it was developed specifically for aircraft applications performed at Airbus. The matrix resin was developed to ensure an optimal translation of the carbon fiber properties whilst delivering outstanding fracture resistance. The sample plates were produced

by Aernnova Composites using the liquid water-based silicone-containing release agent Frekote® C-600 in order to obtain smooth surfaces.

Regarding the structural layout, CFRP monolithic structures were manufactured according to the Airbus AIPS 03-02-019 standard for CFRP ("Manufacture of monolithic parts with thermoset prepreg materials"). For the fracture toughness testing, the adherends consisted of eight unidirectional plies and their layup sequence was $[0_2, \pm 45]_s$ according to the AITM 1-0053 standard [9]. A release film—25 mm in length for the contaminated samples and 30 mm in length for the contaminated/aged samples—was inserted at one end of the sample prior to bonding to obtain an initial delamination for the fracture toughness tests.

The specimens used in the centrifuge tests had a stamp-to-plate configuration. The modular test stamps bonded to the CFRP adherends consisted of an aluminum (EN AW-2007) adherend screwed onto a body of mass made of copper. The CFRP adherends were manufactured from the M21E/IMA prepreg material. The layup sequence of the panels was $[(0/90/45/\text{-}45)_3]_s$.

For the adhesive bonding of the adherends, a film adhesive was used instead of a paste in order to standardize the thickness and increase the reliability of the results. Specifically, the film adhesives FM 300 K and FM 300-2 from Cytec® (0.20 and 0.25 mm thickness, respectively) were used for the production and the repair scenario, respectively.

## *2.2.2 Sample Geometries*

### 2.2.2.1 Coupons

For the mode-I fracture toughness tests, a double cantilever beam (DCB) specimen was used to mirror the relevant geometry and the loading of the adhesive joint. A DCB specimen consists of rectangular adherends bonded along their length, incorporating a region of non-adhesive release film at one end for the introduction of the initial crack in the bondline during testing (Fig. 2.1a). For the mode-II fracture toughness tests, an end notched flexure (ENF) specimen was used. Similar to the DCB specimens, ENF specimens also consist of rectangular adherends, but with a longer pre-crack that is embedded through the width at the end of the specimen to accommodate the sliding deformation of the adherends that result from the flexural loading (Fig. 2.1b). In order to provide crack growth stability, the initial crack length was considered to be equal to 70% of $L/2$ [10, 11]. The test specimens were cut from the residual part of the mode-I specimens.

Finally, the specimen for the centrifuge tests comprised a rectangular composite plate (adherend) bonded to a metallic cylindrical stamp using a technically relevant adhesive system. The test stamps had a diameter of 10 mm on the bonding face. The samples were cut to the desired size by dry diamond cutting. The final dimensions of the CFRP adherends were 25 mm × 25 mm × 4.4 mm.

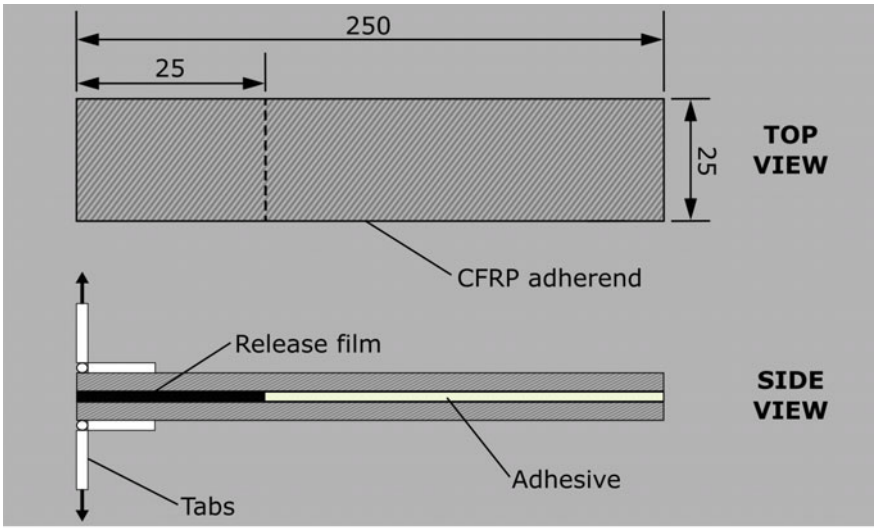


a)

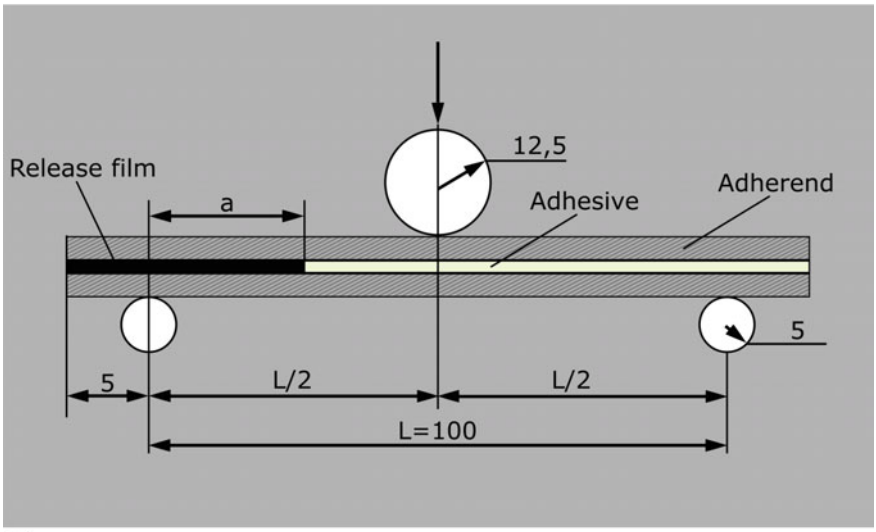


b)

**Fig. 2.1** Geometry, dimensions and boundary conditions of **a** DCB coupon and **b** the ENF coupon

#### 2.2.2.2 Scarfed Samples

As already stated, the two main relevant scenarios for CFRP adhesive joint quality assurance are manufacturing, when the joints are first bonded during aircraft construction, and maintenance, when aerostructures are repaired. Scarfed joints were used for the second scenario. When damage is detected, the aircraft part is locally scarfed

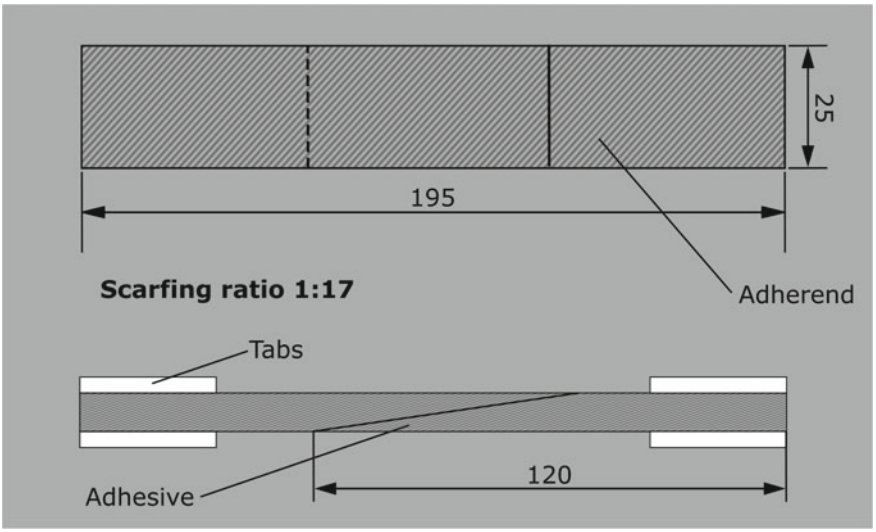


**Fig. 2.2** Geometry and dimensions of the scarfed sample

to remove the damaged outer layers, which are then substituted with a patch that is bonded over the scarfed area in order to restore the load-carrying capacity.

The scarfed samples used in this work were rectangular and consisted of two CFRP plates scarfed by milling with a ratio of 1:17 (Fig. 2.2).

#### 2.2.2.3 Panels

The individual aerospace component parts considered here were two stiffened panels: A flat panel with a laminated skin and two laminated T-stringers for the production scenario, and a curved panel with a laminated skin and two laminated Ω-stringers for the repair scenario. The stringers were spaced at equal distances on the panels.

The dimensions of the panel and the T-stringers are given in Fig. 2.3. The dimensions of the Ω-stringers are 800 mm × 100 mm × 33 mm (Fig. 2.4).

## 2.3 Manufacturing

### *2.3.1 Adherend Manufacturing*

The CFRP laminates for the coupons were manufactured using the automated tape laying (ATL) technique (Fig. 2.5a). The diagram showing the applied vacuum bag

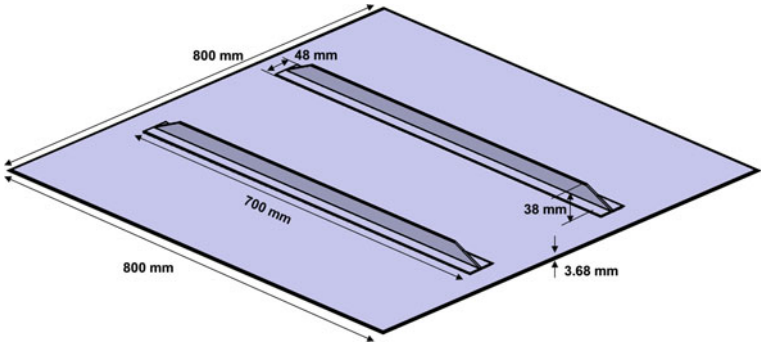


**Fig. 2.3** Geometry and dimensions of the flat stiffened panel

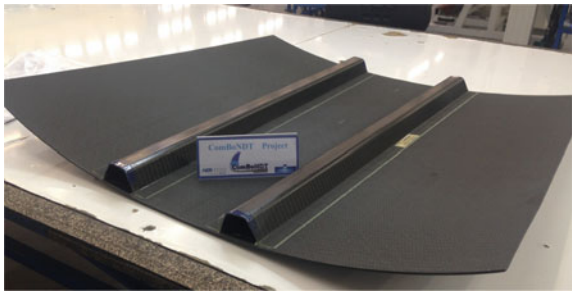

**Fig. 2.4** Curved stiffened panel with a laminated skin and two laminated Ω-stringers

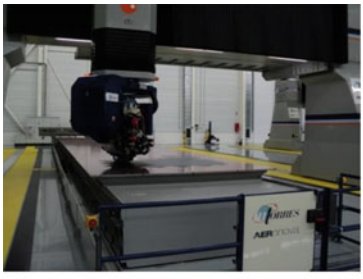

a)

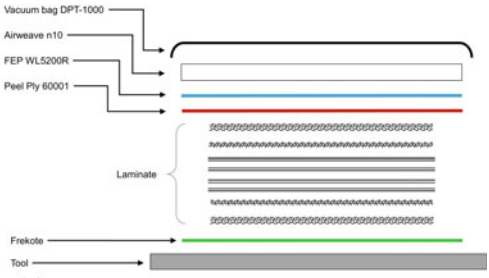


b)

**Fig. 2.5** **a** Photograph showing the automated tape laying process of the laminated panels; **b** diagram of the vacuum bag

is given in Fig. 2.5b, while Fig. 2.6 shows the panels placed inside the autoclave as well as the cutting of the panels.

The CFRP material for the scarfed samples was also manufactured by Aernnova Composites, as described previously, and was then delivered to Fraunhofer IFAM. The CFRP plates were scarfed with a ratio of 1:17 by milling and were then manually ground and cleaned with methyl ethyl ketone (MEK) to remove any handling

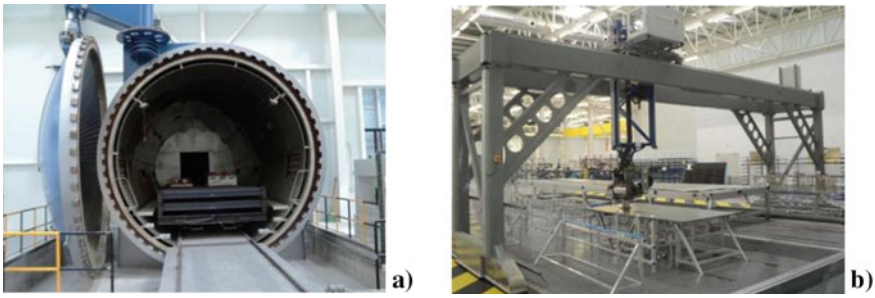


**Fig. 2.6** Photographs showing **a** the panels inside the autoclave and **b** the cutting of the panels

contamination from thermoplastic residues resulting from the milling process. Lastly, the samples were cut to the final size using dry diamond cutting (Fig. 2.7).

The laminated skin for the flat panels (Fig. 2.8a) was manufactured using the same process as was applied for the laminates of the coupons. For the manufacturing of the T-stringers, the web was shaped by joining two C-shaped preforms that had been manufactured using the ATL technology. First, a flat panel was laminated and placed on a hot-forming tool to obtain the C-shape. After that, both C-shaped preforms were joined. Finally, the stringer was trimmed to obtain the six T-stringers with the required dimensions. The T-stringers are shown in Fig. 2.8b.

In the curved stiffened panels, the Ω-stringers were first manufactured using a specific shaping tool (Fig. 2.9). As the skin was curved, a difference in the orientation

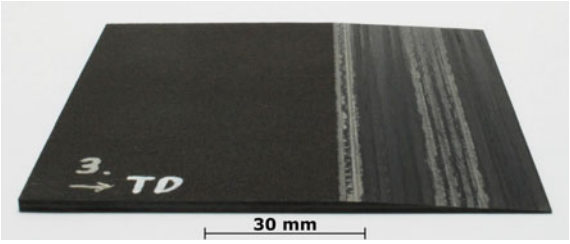


**Fig. 2.7** Overview of scarfed sample after milling

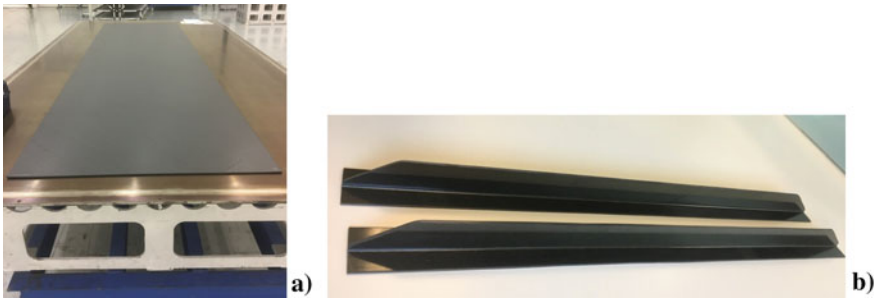


**Fig. 2.8** Photographs showing **a** the flat laminated skin before being placed into the autoclave and **b** the T-stringers

**Fig. 2.9** Photograph showing the Ω-stringers inside the shaping tool

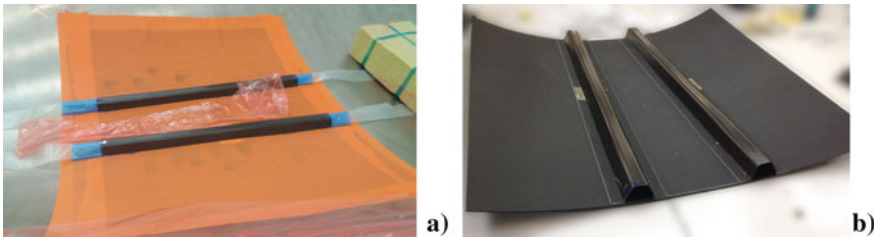


**Fig. 2.10** Photographs showing **a** the preparation of the final curing for the curved panel and the Ω-stringers and **b** the curved and stiffened panel

of the Ω-stringers was considered. The bonding of the Ω-stringers with the skin was done immediately after the manufacturing of the skins. Once the stringers had been placed in their respective positions, the preparation for the final curing cycle started. In addition to the added tubular bags, the panel needed to be protected before entering the curing cycle (Fig. 2.10a). Special attention was paid to the adaptation of the complicated geometry parts to the vacuum bag during the pre-compaction. The curved and stiffened panel is shown in Fig. 2.10b.

### *2.3.2 Adherend Pre-bond Contamination*

Implementing the concept for quality assessment during joining processes, e.g. as applied in the ComBoNDT project, requires the development of ENDT technologies for their integration into adhesive bonding process chains in aircraft production as well as for in-field repair. Such implementation is based on the identification and definition of all test scenarios to be considered and investigated; therefore, possible quality-relevant contaminants with high relevance for all, or at least for

the majority, of aerospace applications must be identified. Following this decision, a detailed description of the sample preparation, including the surface contamination, was prepared in order to guarantee a precise and reproducible sample preparation process, which is an important key element in the success of the entire approach, as highlighted during the ComBoNDT project. Table 2.2 presents more details on quality-relevant scenarios affecting CFRP adherends or adhesive layers in adhesive joints investigated during the ENCOMB [8] or ComBoNDT [5] projects; a more detailed description is provided in the following sections.

#### 2.3.2.1 Production Scenarios

Most aircraft produced nowadays contain a significant number of components made of CFRP, and therefore require the adhesive bonding of CFRP in manufacturing, which further emphasizes the need for complete and reliable quality assurance concepts using ENDT techniques. Three different contaminations were investigated in detail, namely release agent (scenario RA), moisture (scenario MO) and (human) fingerprint (scenario FP).

During the molding process of the composite panels, silicone (Si)-based release agents are used to facilitate the easy removal of the component from the mold. A Si-containing contamination on the CFRP surface caused by release agent residue hinders the adhesion of the adhesive to the substrate [1, 4, 7].

The release agent used was Frekote® 700NC. This is an Si-based liquid that needs to be removed from the CFRP surface before the bonding process because it prevents wetting and adhesion. Therefore, it is necessary to detect possible residues on surfaces prior to adhesive bonding. The release agent was applied to the CFRP surfaces by dip-coating with fixed immersion times and fixed withdrawal speeds. Different concentrations of Frekote® 700NC in heptane were used to yield different degrees of contamination. After the dip-coating of the adherend, the polymerization of the release agent was allowed to occur by drying for 30 min under ambient conditions followed by a heat treatment for 60 min in an oven at 80 °C. The first tests used to yield the desired amounts of Si-containing contaminations on the surface were conducted with solutions of Frekote® 700NC in heptane with the following concentrations (vol%): 1, 2, 3, 4, 5 and 8%. Based on the results of the preliminary tests (X-ray photoelectron spectroscopy measurements and mechanical tests with lap shear specimens), one of the two CFRP adherends per joint was intentionally exposed using dip-coating solutions with the following volumetric concentrations: 1, 2, and 4% of Frekote® 700NC in heptane.

Pre-bond moisture penetration into a composite adherend can occur via either air humidity or direct contact with liquid water. CFRP panels often undergo several pre-treatment procedures, such as wet abrasion and the water brake test, to ensure the effectiveness of the cleaning procedure [4, 7]. Although precautionary measures are implemented, such as using large autoclaves to remove moisture by heat-drying, the problem persists due to the ubiquity of water, e.g. in the surrounding atmosphere, and the limitation of water removal from the bulk of the CFRP thermoset resin through

**Table 2.2** Quality-relevant scenarios affecting a CFRP adherend or an adhesive layer in an adhesive joint as assessed in the European joint research projects ENCOMB [8] and ComBoNDT [5]. In each scenario, the formation and properties of at least one interphase region (close to one of the adherends) is impaired as compared to a joint prepared following the qualified joining process

| Quality-relevant scenario | Technological implementation and denotation | | Affected joint region | Comment |
|---|---|---|---|---|
| | ENCOMB [8] | ComBoNDT [5] | | |
| Reference (during production of the joint) | **X ("RE")** grinded down to fibers | **X ("RE")** grinded | Following the qualified bonding process | ComBoNDT [5]: P-RE (slightly grinded) and R-RE (grinded down to fibers) for production and repair scenarios, respectively |
| Release agent (during production of the joint) | **X ("RA")** higher amount | **X ("RA")** lower amount | CFRP surface covered by nanoscale film | Same silicone-containing agent used in ENCOMB and in ComBoNDT |
| Moisture (during production of the joint) | **X ("MO")** | **X ("MO")** | CFRP surface covered by nanoscale water film; moist CFRP bulk | |
| Fingerprint (during manufacture of the joint) | – | **X ("P-FP")** (following DIN ISO 9022-12) | CFRP surface covered by (dried) aqueous film | Artificial hand perspiration solution, according to DIN ISO 9022-12 [12] |
| Thermal impact (during joint application; repair scenario) | **X ("TD")** (thermo-oxidative) | **X ("TD")** (thermal) | CFRP surface thermo-oxidatively affected during application; CFRP bulk thermally affected | Removal of oxidatively affected surface region by grinding only in ComBoNDT |
| Exposure to components of hydraulic oil (during joint application; repair scenario) | **X ("HF")** (immersion in aqueous extract of oil) | **X ("R-FP")** (fingerprinting of hydraulic oil) | CFRP surface covered by a film | Different liquids used in ENCOMB and ComBoNDT |
| De-icer (during repair of the joint) | – | **X ("DI")** | CFRP surface covered with salt particles | De-icer liquid based on potassium formate |

(continued)

**Table 2.2** (continued)

| Quality-relevant scenario | Technological implementation and denotation | | Affected joint region | Comment |
|---|---|---|---|---|
| | ENCOMB [8] | ComBoNDT [5] | | |
| Faulty curing of adhesive (during repair of the joint) | – | **X ("FC")** | Adhesive layer; interphases to adherends | Initiated by selective pre-curing of the adhesive |

diffusion as it is intercepted by the fiber layers. Moisture uptake mainly affects the properties of the matrix, resulting in swelling and the development of stresses large enough to pull the matrix away from the fiber [4, 7, 13]. Moreover, moisture also affects the adhesion properties [13]. CFRP can absorb moisture by up to 1.5–2.0 wt%. The range for concern at production sites often goes up to 0.5 wt%. A higher moisture uptake needs to be avoided because it negatively influences the adhesion properties and leads to a loss of performance of both the CFRP as well as the adhesive bond.

The preparation of moist CFRP samples was performed following two different procedures with different environmental conditions: One for use in the development of ENDT monitoring technologies for the quality assurance of adherend surfaces and the second one for the measurement of the mechanical properties of the bonds and for the further development and adaptation of ENDT technologies for the quality assurance of adhesive bondlines. Regarding the first category, the samples were contaminated in a defined climate that was established in small boxes in an oven at 70 °C. The humidity in the boxes was adjusted using beakers of demineralized water (MO-3) and saturated salt solutions (MO-1 and MO-2), which were placed in the boxes together with the samples until a constant weight of the samples had been achieved. The beakers in the boxes contained the following aqueous liquids in terms of saturated salt solutions: $MgCl_2 * 6H_2O$ saturated solution for MO-1, resulting in an approximately 30% relative humidity (RH); NaCl saturated solution for MO-2, resulting in an approximately 75% RH; and pure demineralized water for MO-3, resulting in an approximately 99.5% RH.

Clean CFRP samples were dried at 80 °C until they had achieved a mass constancy resulting in the dry weight. Afterward, they were stored in the respective boxes with moist atmospheres until the weight was constant (at least 40 days) and then taken out directly prior to the measurement with the respective surface inspection method. With this method, the following mass uptake of water was achieved:

- 0.4 (±0.2) mass% water for MO-1
- 0.8 (±0.1) mass% water for MO-2
- 1.4 (±0.2) mass% water for MO-3

For the second MO conditioning, the samples were prepared using a different procedure. These adherends were dried in an oven at 80 °C until mass constancy.

They were then stored in a climate chamber (70 °C and with the respective and well-defined relative humidity) for two weeks prior to bonding. After the removal from the climate chamber, the samples were directly bonded. The following RH conditions were adjusted in the chamber:

- 30% RH for MO-1
- 75% RH for MO-2
- 98% RH for MO-3

All the results presented in this chapter refer to the second MO conditioning.

Contamination by fingerprints can occur due to inadequate cleaning of a bonding surface or inappropriate handling after the cleaning process [14, 15]. Fingerprint contamination leads to the formation of thin contaminant films on the bonding surfaces and, ultimately, to a lower adhesion quality [15]. This may occur during both production and repair processes. Even though the occurrence of fingerprints seems to be easily avoidable, they are often responsible for adhesion failures, and therefore the detection of fingerprints is an essential requirement for an appropriate quality assurance approach.

Concerning the samples with fingerprint contamination to be investigated for the production scenario, the preparation was performed using a standardized salty fingerprint solution (artificial hand perspiration solution) according to DIN ISO 9022-12 [12]. This liquid formulation contains sodium chloride, urea, ammonium chloride, lactic acid, acetic acid, pyruvic acid, and butyric acid dissolved in demineralized water. Samples were prepared by manually applying this solution onto a surface area of the samples that correspond to the size and extent of a wet fingerprint. Different degrees of contamination were achieved by using different dilutions (with demineralized water) of the FP solution:

- 10% FP solution for P-FP-1
- 50% FP solution for P-FP-2
- pure FP solution for P-FP-3

Finally, in addition to the single contamination cases described above, the occurrence of a combined contamination case was also considered. Combined contaminations for the production scenario included the combination of release agent and fingerprint contaminations (RA+FP). Two levels of contamination were investigated:

- Low-level contamination (RA1+FP3): level RA-1 of release agent followed by the application of level FP-3 salt-based fingerprint solution.
- Medium-level contamination (RA2+FP3): level RA-2 of release agent followed by the application of level FP-3 salt-based fingerprint solution.

#### 2.3.2.2 Repair Scenarios

In the second field of feasible application scenarios, distinct composite "repair" cases were defined, implemented, and examined. Hereby, the effects of contacting adherend surfaces with either of the two contaminant materials de-icing fluid or hydraulic oil

(applied in a fingerprinting process) were examined in detail. The third scenario dealt with thermally degraded CFRPs and aimed to account for CFRP parts that may have been exposed to heat (fuselage parts or alighting gear, for example, or aircraft structures that affected by lightening impact) and are then subjected to a mechanically abrasive surface pretreatment process. A fourth scenario that was investigated comprised a faulty curing of an adhesive that is then applied to distinct pretreated adherend surfaces. In the following, these technologically relevant contamination issues will be assessed in more detail.

In winter, airports use a de-icer to maximize runway friction during plane taxiing. Runway de-icing fluid is one of the most commonly encountered fluids to which aircraft structures may be exposed, as it can be swirled up from the runway and onto the outer parts of the aircraft [16]. During the patch repair of composite parts, inadequate cleaning can result in residues or the transfer of de-icing fluid onto adherend surfaces. After drying, potassium formate, which is present in the de-icing fluid, forms a thin layer on the CFRP part, thus affecting the bonding quality.

The de-icer used (DI scenario) was SAFEWAY® KF from CLARIANT, which contains potassium formate (KF) as the freezing point depressant. It was diluted with demineralized water to obtain solutions with the following concentrations in vol%: 2, 5, 7, 10, 30, and 50%. It was applied to the surfaces by dip-coating in the respective aqueous solution; finally, drying was performed in an oven for 2 h at 40 °C in air. Subsequently, acclimatization at room temperature was allowed for at least 24 h.

With the aim of narrowing the applied range of de-icer solution concentrations, three lap shear specimens comprising one contaminated adherend each were manufactured for each of these DI concentrations, and these were then used for adhesive bonding and subsequent mechanical testing. A significant loss in bond strength was observed for contamination levels characterized by surface concentrations of approximately 4 at.% potassium as measured by XPS. The fracture pattern also showed an impact when potassium surface concentrations of approximately 4 at.% were present. Based on these preliminary tests, it was decided to assess such samples in more detail; these were obtained using de-icer dip-coating solutions with the following concentrations for the ComBoNDT final coupon level samples: 2, 7, and 10% de-icer in demineralized water.

Moreover, CFRP aircraft parts may be exposed to high temperatures during service, for example, when fuselage parts are exposed to lightning [17], which causes local overheating and damage to the matrix or the wing parts situated close to the engines. Damage can also be caused by an overheating of an aircraft part by an external source of heat (gas, liquid, beam, etc.) that has inadvertently been placed near the aircraft. Besides affecting the mechanical properties of the structural parts, the thermal impact on and resulting degradation of the CFRP parts might also affect bonding in a repair situation.

For the sample preparation, all thermal impact treatments were carried out in an oven with air circulation. The samples (subsequently denoted as TD samples) were placed inside the oven and then underwent the heating phase at different temperatures. Once the indicated temperature was reached, the samples remained inside the oven for 2 h. Prior to both the surface inspection and the subsequent steps of the bonding

process, all samples were grinded down to the fibers (using Si-free sandpaper, grit size 120). A significant loss in bond strength (lap shear specimens) was observed for the samples treated with 280 °C. In a comparison with joints prepared from adherends that had not suffered such a thermal impact, the fracture pattern demonstrated an impact from a heat treatment of 260 °C. Based on these results, the following three different temperatures were used to realize three different levels of thermal impact (TD):

- 220 °C for TD-1
- 260 °C for TD-2
- 280 °C for TD-3

Concerning a further feasible contamination scenario, oily fingerprints can accidentally be applied to CFRP bonding surfaces when, for example, a worker wears gloves while working in an area where hydraulic oil is used and afterwards touches a bonding surface. Even though this contamination scenario seems easily avoidable, it is nevertheless of great importance in the field of aircraft repair because such a transfer of oil is unlikely to be detected during a visual inspection. Concerning the sample preparation for the repair scenario, fingerprints containing Skydrol 500B-4 hydraulic oil from Eastman were applied to the surfaces using a plastic finger. The oil was diluted in heptane to obtain formulations with the following contamination concentrations in vol%:

- 20% for a low level (denoted as R-FP-1)
- 50% for a medium level (R-FP-2)
- 100% for a high level (R-FP-3)

In order to achieve adequate adhesive bonding processes, it is important that all adhesive-related parameters, like pot life and curing times, comply with regulations as well as the specifications of the qualified bonding process. If the adhesive is out of specification with respect to its pot life due to, e.g., too high temperatures in the working area, the result can be weak or kissing bonds in the resulting joint. In this scenario, the bonded joint does not contain any foreign materials or contaminants that have erroneously remained after the cleaning, pretreatment, or conditioning steps. Instead, the loss of performance of the bonded joint is due to irregularities affecting the adhesive material that was used in the manufacturing process of a limited number of joints.

Regarding the sample preparation, a faulty curing of the adhesive was initiated through a selective pre-curing of an adhesive that was subsequently introduced into the bonding process. In the resulting selected and pre-cured areas, the bond strength may be reduced drastically, possibly due to its impeding any force transfer. This scenario will represent the cases of weak and kissing bonds. Three levels of pre-curing resulting in a faulty curing (FC) of the adhesive were realized:

- a slight pre-curing for FC-1
- a medium pre-curing for FC-2
- a strong pre-curing for FC-3

Finally, besides the single contamination cases described above, a combined contamination case was also considered. Combined contaminations in the repair scenario include the combination of thermal degradation and de-icing fluid (TD+DI), whereby two levels of contamination were investigated:

- Low level of contamination (TD1+DI1): Thermal degradation at 220 °C for 2 h followed by dip-coating in the DI1 concentration of the de-icing fluid solution.
- Medium level of contamination (TD1+DI2): Thermal degradation at 220 °C for 2 h followed by dip-coating in the DI2 concentration of the de-icing fluid solution.

### *2.3.3 Bonding*

For the production scenarios, the samples described in this book were bonded in an autoclave using the adhesive FM® 300 K (0.2 mm) from Cytec® following the curing cycle shown in Fig. 2.11. The heating rate (starting from room temperature) was 3 K/min up to 175 °C. The pressure was 3 bars and the final temperature of 175 °C was held for 1 h.

Plates with the dimensions 30 cm × 30 cm and 30 cm × 15 cm were bonded and afterwards cut into the desired sizes for measurements with the respective measuring techniques as well as for mechanical testing in the specified geometries. The cutting was performed dry (diamond cutting) to prevent any contamination of the cleaned surfaces as might be the case when using cooling liquids. After cutting, the surfaces were cleaned again with isopropanol (IPA) soaked tissues. Figure 2.12 shows the preparation of the samples for bonding in the autoclave (at Fraunhofer IFAM facilities).

For the repair scenarios, all the samples were bonded in the autoclave using the adhesive FM® 300-2 (0.25 mm), which is specially designed for bonded repair. The

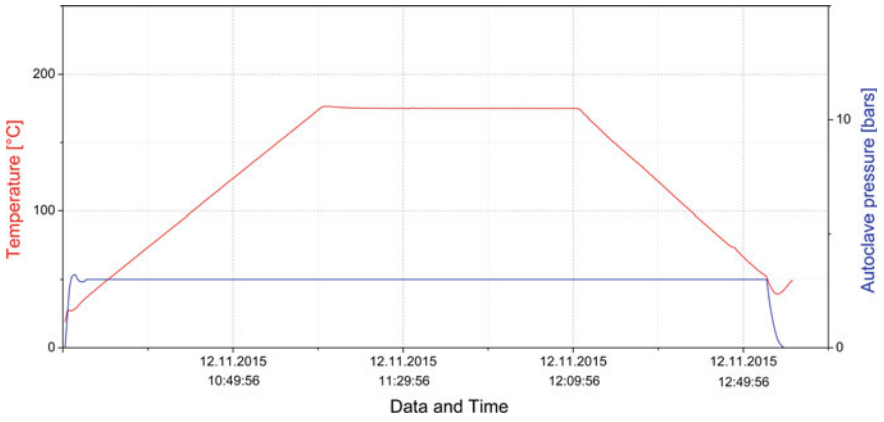


**Fig. 2.11** Autoclave thermal and pressure cycle for bonding production samples with adhesive FM® 300 K


**Fig. 2.12** Photographs showing the preparation of samples for bonding **a** in the autoclave and **b** using a vacuum bag

respective curing cycle is shown in Fig. 2.13. The CFRP plate sizes and the cutting of the samples into the final sizes after the bonding were as described for the production of the samples.

For the bonding of the centrifuge samples (Fig. 2.14a), the film adhesive was hole-punched to a diameter of 10 mm and then deposited onto the test stamp (cleaned by sonication for 5 min in isopropanol), which was then placed onto the CFRP sample (Fig. 2.14b). The production samples bonded with the FM 300 K adhesive were cured in an autoclave using a custom-made curing device at 3 bars and 175 °C for 60 min (heating up to 175 °C in 60 min, cooling down to room temperature in 60 min). The repair samples bonded with the FM 300-2 adhesive were cured at 2 bars and 121 °C for 90 min (heating up to 121 °C in 30 min, cooling down to room temperature in 60 min).

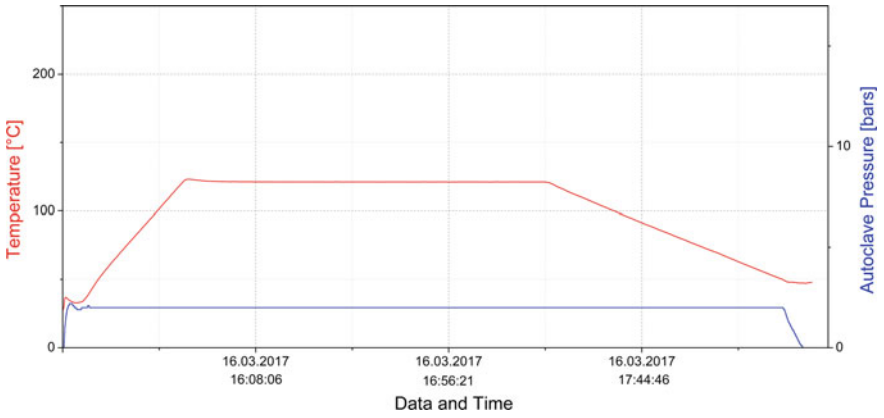


**Fig. 2.13** Autoclave thermal and pressure cycle for bonding repair samples with the adhesive FM® 300-2

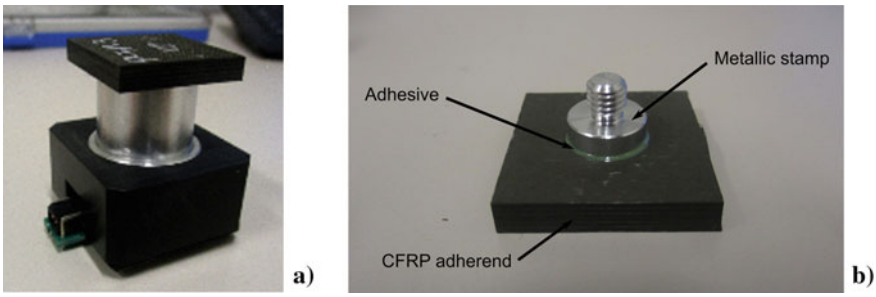


**Fig. 2.14** Photographs showing the stamp-to-plate specimen used in the centrifuge tests; **a** full specimen configuration and **b** metallic stamp bonded to the CFRP adherend

## 2.4 Experimental Procedure

### *2.4.1 Characterization of CFRP Adherend Surfaces by Reference Methods*

Spectroscopic surface characterization was performed on the CFRP adherends before the adhesive bonding to verify the contamination level obtained by the contamination procedure. X-ray photoelectron spectroscopy (XPS) was used as a spectroscopic reference method, and XPS measurements were performed on detached and cut plates in the state "as delivered" on three different surface positions.

X-ray photoelectron spectroscopy (XPS) is a widely used surface analysis method for the characterization of the elemental and chemical composition of a sample surface, which is positioned inside a vacuum system. XPS is based on the photoelectric effect and enables the study of the energy distribution of the photoelectrons emitted by X-ray irradiated compounds [18]. Monochromatic soft X-rays irradiate the sample surface, and upon interaction with the sample material electrons are emitted, mainly from the atomic core levels. These ejected electrons have discrete kinetic energies, and the portion of electrons passing the electron energy analyzer is detected within the photoelectron spectrometer. Signal intensities are given by the number of emitted photoelectrons as a function of the photoelectron kinetic energy. A high vacuum environment is required to enable the emitted photoelectrons to be analyzed without interference from gas-phase collisions, and in cases of electrically non-conducting surfaces special care is taken to control electrostatic surface charging.

### 2.4.2 Characterization of CFRP Bonded Samples by Reference Methods

Ultrasonic testing is considered a conventional NDT technique for the quality control of components. This technology is widely used for composite material inspection in aeronautics as well as in other domains. It is thus considered as a standard method by end users.

Within the ComBoNDT project, the aim of the ultrasonic inspection was to check the integrity and quality of the produced bonded samples. Indeed, according to the literature and also with regards to the context of the project, a "weak bond" is not expected to be detectable by conventional NDT methods. Otherwise, a common interpretation of the obtained data is that such a bond is considered a bond with defects (such as voids, porosity, gap-like disbonding) rather than as a possible weak bond. Therefore, within the framework of the characterization using ultrasonic testing as a reference method for the bonded samples, one issue was proving that the contamination and bonding processes do not lead to such defects. This information, in combination with the results of the terminal destructive mechanical testing (i.e. strength and fracture pattern), is required in order to consider the respective joints as samples with weak bonds.

Three categories of samples were investigated:

(a) Coupons were widely used by all the project partners in order to develop their ENDT technology, and thus it is of great importance that the quality of these samples is known. The obtained dataset comprises results from more than 360 samples.
(b) Multi-contaminated samples were used to increase the maturity of the ENDT technologies.
(c) Curved specimens were also tested. In this case, the curvature of the samples led to challenges in the signal reception, which rendered the inspection of these samples more prospective than quantifying.

The ultrasound-based inspections were performed in the Airbus laboratory using an M2M ultrasonic generator and a 6-axis mechanism (Fig. 2.15b, c). The immersion configuration was selected to maximize the signal quality. Samples were placed in consistent groups in the water tank on metal beams (Fig. 2.15d). The water path for passing the oscillation from the sonotrodes to the sample, i.e. the distance between the probe and the samples, was set to 40 mm on average. Two different phased array probes were used for the inspection (Fig. 2.15a). The characteristics are given below, with the trajectory parameters for each:

– 5 MHz linear probe, 64 elements, 1.0 mm pitch, 64 mm of aperture, 10 mm elevation, flat focusing; linear scanning; scanning step: 2 mm (standards), increment 30 mm
– 10 MHz linear probe, 64 elements, 0.5 mm pitch, 32 mm of aperture, cylindrical focusing (R = 40 mm); scanning step: 1 mm, increment 20 mm (i.e. 33% overlap)

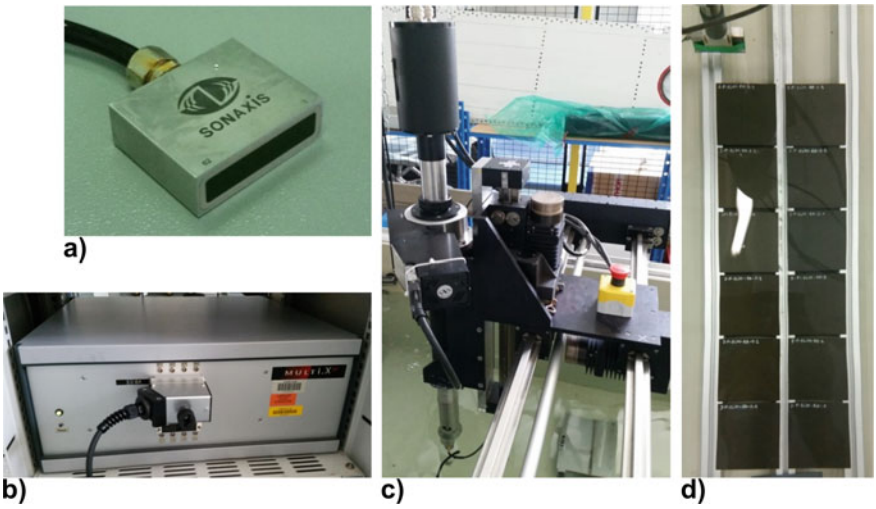


**Fig. 2.15** Overview of the ultrasonic inspection setup; **a** example of a phased array probe; **b** ultrasound generator for emission and reception (M2M MultiX); **c** water tank and the 6-axis mechanism used to scan the parts; and **d** typical placement of the samples in the water tank for the inspections

The 5 MHz probe corresponds to Airbus standards. It was important to check that it is not possible to highlight any contamination-induced defects using current production tools. The 10 MHz probe was chosen because it is more accurate due to its higher central frequency and the smaller element size.

For each probe, different settings were used for the production samples and the repair samples. The global gain of the signal and the time correction gain (TCG) are slightly different between scenarios. This is mainly due to the bond material, which is different in each case and thus induces different ultrasonic responses.

In order to display ultrasonic cartographies, software settings (or gates) are necessary. A typical B-scan and A-scan are given in Fig. 2.16a with the gate display. Three main echoes can be observed, namely the front wall echo (with the gate or, respectively, obtained signal dataset denoted as "FWE"), bond echo ("Bond") and back-wall echo ("BWE"). All gates are synchronized using a synchronization gate tracking the entry echo. These gates can subsequently be used for the analysis. The respective details are

- "FWE" is the maximum of the front wall echo. It can be used to check the acquisition quality and to highlight surface defects.
- "g+" records the highest echo after FWE. In this case, it is typically the bond or the back-wall echo. The signal from this gate is particularly useful to compare the echoes.
- "Bond" is centered on the bond echo and tracks its maximum.
- "BWE" is centered on the BWE and tracks its maximum.

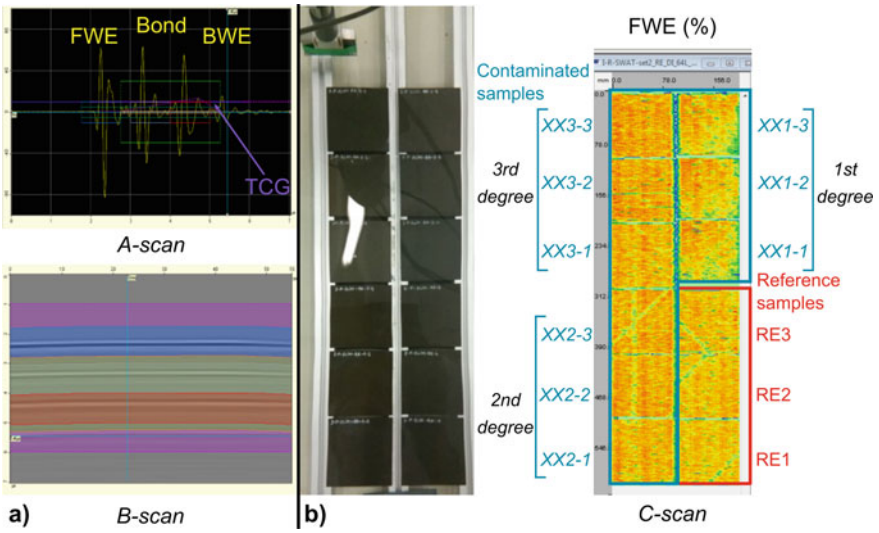


**Fig. 2.16** Use and display of the ultrasound results from gates related to the front wall echo (FWE), bond echo (Bond), and back-wall echo (BWE); **a** typical A-scan and B-scan with gates setting display and **b** example of cartographies in amplitude for bonded coupon coupons with the corresponding sample positions

These gates are used to generate cartographies, also called C-scans, where the amplitude (given in %) or the time-of-flight (TOF, given in μs) of the recorded echo is displayed on the inspection plan (for an example of amplitude cartography see Fig. 2.16b). Samples are always placed in the same way with the references situated on the bottom right and the contaminated samples in the remaining spaces. For each set of samples, the origin is taken at the top left corner for the defect positioning.

In order to be complete, there must be precision on the phased array acquisition mode. Two different pulse-echo modes were used:

- The linear scanning (LS) mode, which consists of emitting a group of elements (E10 typically) and then receiving the same group of elements (R10). This configuration increases the scan accuracy. A single point focusing (SPF) can be added to direct the ultrasonic beam along the bondline, for example.
- The PaintBrush (PB) mode with the additional surface adaptative ultrasonic laws (SAUL) option, which consists of emitting with all the elements (E64) and then summing the responses by groups of elements (R10 for the 5 MHz probe and R16 for the 10 MHz probe). Such an investigation is faster but can lead to "strip-like" marks within the cartographies. The SAUL algorithm was also used in some specific cases. This option is particularly interesting for curved parts or to achieve a higher tolerance to a misalignment between the probe and the coupons.

## 2.5 Mechanical Testing

### *2.5.1 Fracture Toughness Testing*

#### 2.5.1.1 Mode-I Testing

Mode-I fracture toughness tests were conducted with double cantilever beam specimens according to the standard AITM 1-0053 [9] using a Tinius Olsen H5KT universal testing machine with a load cell of 5 kN under ambient conditions (25 °C, 55% RH) and under constant displacement control. Loading was applied to the DCB specimen via metallic piano hinges bonded to the adherends at one end. In order to avoid any influence of the incorporated release film, the specimen was preloaded until an initial crack length of 10–15 mm was achieved. The pre-cracked specimens were then loaded continuously by opening forces until a total propagated crack length of 100 mm was reached. After that, the test was stopped, and the specimen was unloaded. Six specimens per scenario were tested in this manner. During the crack propagation, the load and crosshead displacement of the test machine was recorded continuously. A traveling microscope was used to facilitate the visual measurement of the crack length. Figure 2.17 illustrates the mounting of a specimen onto the tensile testing machine during the mode-I test.

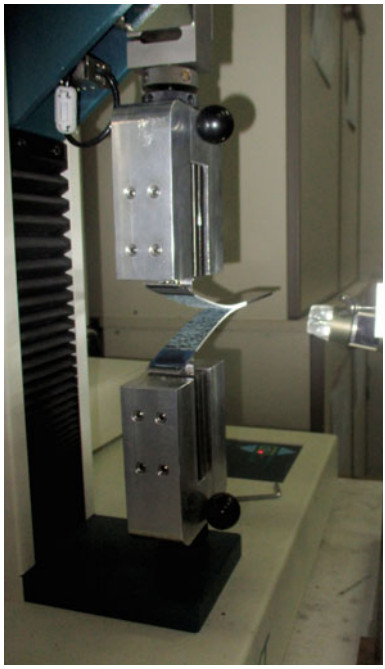

**Fig. 2.17** Photograph showing a DCB specimen under mode-I loading

The AITM 1-0053 standard specification specifies the area method to determine the mode-I fracture toughness energy $G_{IC}$ of CFRP bonded joints [9]. The crack extension is related directly to the area enclosed between the loading and unloading curves:

$$G_{IC} = \frac{A}{a \times w} \times 10^6 \left(J/m^2\right) \tag{2.1}$$

where

*A* is the energy required to achieve the total propagated crack length (J) (integration of the area of the load-crosshead displacement diagram)
*a* is the propagated crack length (mm) ($a = a_{final} - a_{initial}$)
*w* is the width of the specimen (mm)

The most popular approach to investigating delamination mechanisms in mode-I tests is the examination of fracture surfaces. Therefore, in order to accurately assess the causes of bondline failure, the fracture patterns were examined after the tests based on a visual inspection supported by photography. The classification, identification, and characterization of the failure mode of the CFRP bonded joints were conducted according to the ASTM D5573 standard [19]. For increased accuracy, a grid drawn on a clear film placed over the failure surface was used and the square areas showing a certain type of fracture pattern were counted, providing input to calculate the area percentage attributed to each failure mode. The main failure modes that were observed for the tested CFRP adhesive joints are schematically described in Fig. 2.18:

a. Adhesive (ADH) failure, which occurs when a separation takes place at the adhesive/adherend interface (respectively, within the three-dimensional adhesive/adherend interphase).
b. Cohesive (CO) failure, which results when a separation takes place within the adhesive.
c. Fiber tear (FT) failure, which is perceived when a failure occurs exclusively within the matrix of the CFRP adherend, resulting in the appearance of fibers on both fracture surfaces.
d. Light fiber tear (LFT) failure, which follows when a failure occurs within the adherend, near the interface characterized by a thin layer of the matrix on the fracture surface with few or no fibers transferred from the substrate to the adhesive.
e. Thin layer cohesive (TLC) failure, which is observed when the separation takes place within the adhesive in proximity to one adherend and not around the mid-thickness area of the adhesive layer.

Usually, a mixed failure occurs and symptoms of several failure modes are observed simultaneously for each tested specimen.

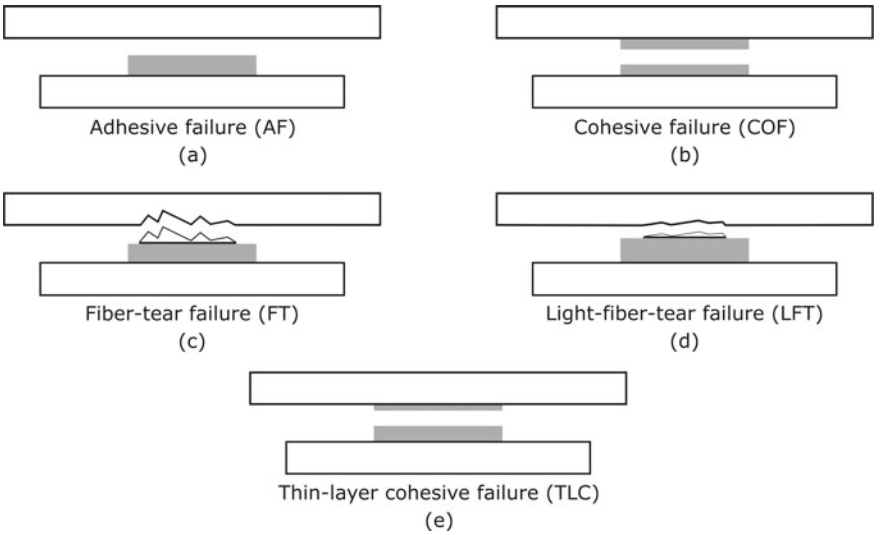


**Fig. 2.18** Schematic representation of the main failure modes of CFRP bonded joints observed after destructive mechanical testing

#### 2.5.1.2 Mode-II Testing

Since there is currently no standardized mechanical test to measure the fracture toughness energy of bonded joints under pure mode-II loading, we decided to use the ENF test, which we have identified as the most convenient mode-II fracture toughness test [16]. Figure 2.19 provides a schematic representation of the ENF test,

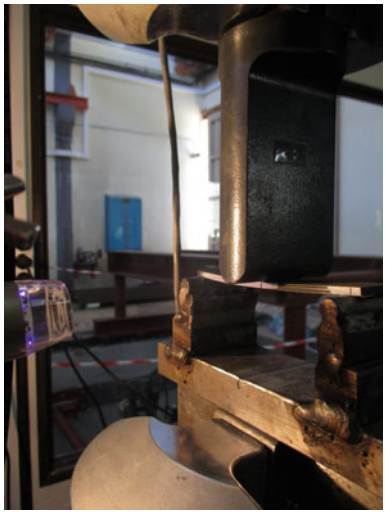

**Fig. 2.19** Photograph showing an ENF specimen under mode-II loading

wherein a pre-cracked specimen is loaded into a three-point bending fixture until the crack propagation onset occurs.

Mode-II tests were conducted according to the AITM 1-0006 standard [20] under a constant displacement rate of 1 mm/min using an MTS universal testing machine with a load capacity of 100 kN. The test specimens were cut from the residual parts of mode-I specimens so that a pre-crack of 35 mm was achieved. Three specimens were tested for each condition within the considered scenarios. In order to facilitate the optical observation of the crack tip and the detection of the crack propagation onset, a digital microscope was used, and a thin layer of white ink was applied to the longitudinal side faces of the specimen.

Both the load applied to the specimen and the crosshead displacement of the test machine were continuously recorded during the test. To calculate the $G_{IIC}$ fracture toughness energy, the following formula was used [20]:

$$G_{IIC} = \frac{9 \times P \times a^2 \times d \times 1000}{2 \times w \times \left(1/4 \times L^3 + 3 \times a^3\right)} \left(\mathrm{J/m^2}\right) \tag{2.2}$$

where

$d$ is the crosshead displacement at onset of the crack propagation (mm)
$P$ is the critical load to start the crack propagation (N)
$a$ is the initial crack length (mm)
$w$ is the width of the specimen (mm)
$L$ is the span length (mm)

#### 2.5.1.3 Centrifuge Testing

Standardized methods only allow the testing of specific bond strength parameters, and the achieved statistics are often limited due to the high cost and work effort required. Additionally, the respective measurements are time and cost-consuming due to complex sample and fixture preparation, single-sample testing, and manual evaluation of the mechanical load and fracture surfaces. Against this background, the novel centrifuge test is introduced in order to overcome these limitations.

Up to eight samples can be measured within 5 min and the measured mechanical properties have a defined accuracy with very good precision and reproducibility. The novel testing is cost-efficient, fast, and reliable. In the ComBoNDT project [5], the information value of mechanical testing was increased as compared to the results obtained from the abovementioned standardized mechanical tests.

The centrifuge testing principle for bonded joints is illustrated in a schematic diagram in Fig. 2.20 [21]. The centrifuge test is based on the physical law of inertia of a body [22]. Due to rotation, a progressively increasing radial centrifugal force is applied synchronously to each of the specimens being tested. The load increase is adjusted through a variation of the rotor's rotational speed.

Across the bondline, the axial centrifugal force acts as a normal tensile force. If the applied load exceeds the tensile strength of the joint, a rupture occurs, and the

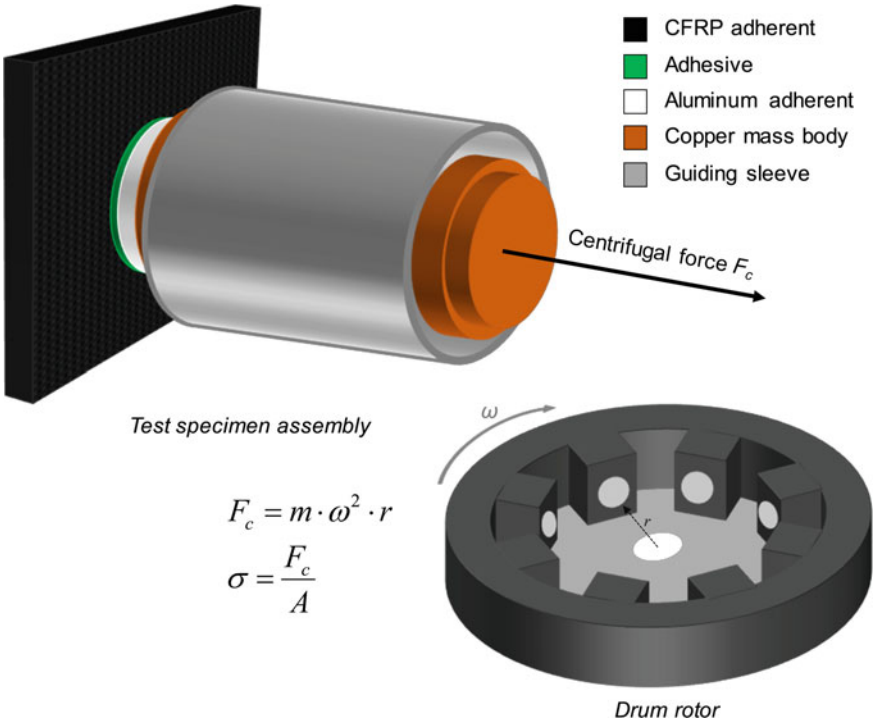


**Fig. 2.20** Diagram highlighting the measurement principle of the centrifuge test

test stamp changes its position within the guiding sleeve. The detachment of the test stamp from the CFRP adherend at the moment of rupture is automatically detected and a position-coded infrared signal is sent from the turning rotor, transmitting the current rotor speed as well as the rupture time [23].

The centrifugal force $F_c$ (N) is derived from

$$F_c = m \cdot \omega^2 \cdot r \tag{2.3}$$

where $m$ (kg) is the mass of the stamp, $r$ (m) is the distance of the test stamp to the rotational axis, and $\omega$ (rad/s) is the angular velocity related to frequency $v$ by

$$\omega = 2 \cdot \pi \cdot v \tag{2.4}$$

Dividing the centrifugal force $F_c$ (which is effective at the time of the adhesive fracture) by the area of the bondline $A$ (mm$^2$), the tensile adhesion strength $\sigma$ (MPa) is derived:

$$\sigma = \frac{F_c}{A} \tag{2.5}$$

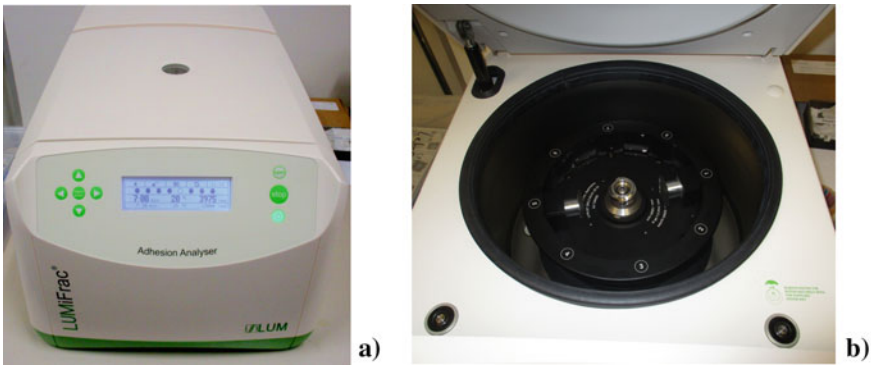


**Fig. 2.21** Photographs displaying the setup for the centrifuge test; **a** the LUMiFrac desktop analyzer and **b** stamp-to-plate test specimens inside the drum rotor

For the preparation of the thus investigated joints, the composite substrates were subjected to contamination with the release agent, moisture, fingerprint, thermal degradation, or de-icing fluid before being bonded to the metallic stamp. The centrifuge tests were carried out using a LUMiFrac desktop adhesion analyzer equipped with an LSFR-ST: 200.42 drum rotor with up to eight testing units (Fig. 2.21). The fully loaded rotor allows for a maximum rotational speed $\omega$ of 13,000 rpm, corresponding to a centrifugal acceleration of 13,715 g [23].

By means of the SEPView software, the desired load-controlled testing sequence was realized. To achieve compatibility with conventional testing machines (in load-controlled mode), the increase in the rotational speed of the rotor was designed to be quadratic. According to Eq. (2.3), a square root-like increase in the rotational speed is accompanied by a linear increase in the centrifugal force [24]. Subsequently, the rotor and centrifuge lid were closed, and the testing procedure was initiated. The duration of each test lasted from 6 to 20 s on average, depending on the contamination scenario. The rupture event was detected online outside the centrifuge using a position-coded and rpm-correlated infrared data transmission from the inside of the testing units mounted in the drum rotor. After testing, high-resolution microscopy images of the failure surfaces of both the CFRP adherend and the test stamp's side were taken and examined with the aim of characterizing the failure patterns.

#### 2.5.1.4 Tensile Testing

Scarfed samples were loaded under ambient conditions (25 °C/48%RH) by tensile stress using an MTS universal testing machine with a load capacity of 100 kN under a constant crosshead speed of 0.5 mm/min (Fig. 2.22) until a final failure (separation) of the two scarfed adherends occurred. Aluminum end tabs (30 mm × 25 mm × 2 mm) were bonded to the ends of the specimens using a two-part adhesive (PM Mega Cryl) in order to achieve a successful and smooth introduction of the load into


**Fig. 2.22** Photograph showing a scarfed specimen under tensile loading

the specimen. Moreover, the end tabs prevented gripping damage to the adherends or premature failure as a result of a significant discontinuity. The load and crosshead displacement were recorded using a computerized data logging system. A total of four tests were performed for each contamination scenario and the failure load was the mechanical feature used for comparing the tested specimens.

Additionally, after the tensile tests, the failure surfaces were examined in order to accurately assess the causes of adhesive joint failure. The ASTM D5573 [19] standard was followed.

#### 2.5.1.5 Environmental Aging

The procedure given in the EN 2823 [25] standard was used to determine the effects of after-bond exposure of the joints to a humid atmosphere on the mechanical characteristics of the contaminated joints. The specimens were exposed without mechanical loading to conditions of 70 °C and 85% RH until the moisture saturation point, which was reached after approximately 65 days of aging.

The specimens to be aged were placed inside an environmental chamber with an embedded pre-crack (Fig. 2.23), which was created a priori through mode-I tests conducted according to the AITM 1-006 standard [20]. Reference and contaminated specimens were subjected to hygrothermal aging using an ESPEC SH-641 environmental chamber for a period of 64–74 days, ensuring that the saturation point was reached.

**Fig. 2.23** Photograph showing CFRP joint specimens inside the chamber during environmental aging

During the hygrothermal aging period, the weight of the specimens was measured at weekly intervals. After the hygrothermal aging, the specimens were stored in sealed containers and tested under mode-II loading conditions within 72 h according to the DIN EN 2823 standard [25].

As a measure of the absorbed moisture, the percental normalized weight gain $M(t)$ was used:

$$M(t) = \left(\frac{w_t - w_0}{w_0}\right) \times 100 \tag{2.6}$$

where

$w_0$ is the initial weight (g)
$w_t$ is the weight at exposure time $t$ (g)

The weight gain achieved with these hygrothermal aging conditions was 0.49–0.71%. Fick's law was used to define the equilibrium conditions in composite materials [25]. The diffusion coefficient $D$ of water is derived from the slope of the linear part of $M(t)$ curve as

$$D = \pi \times \left(\frac{h}{4 \times M_\infty}\right)^2 \times S^2 \left(\frac{\text{mm}^2}{2}\right) \tag{2.7}$$

where

$M_\infty$ is the water uptake at saturation (wt%)
$h$ is the specimen thickness (mm)
$S$ is the slope of the $M(t)$ curve $\left(1/s^{0.5}\right)$.

## 2.6 Experimental Results

### *2.6.1 Spectroscopic Surface Characterization*

To prepare the clean reference samples from the delivered CFRP plates, a thorough cleaning procedure was followed to remove any contaminations or residues remaining from the manufacturing process (Fig. 2.24). Each step was monitored using X-ray photoelectron spectroscopy (XPS) analyses to measure the amount of release agent on the plate surface:

1. Pre-cleaning of the plates with isopropanol (IPA) soaked tissues to remove part of the release agent and any other soluble contaminations, e.g. fingerprints, remaining from the manufacturing process. XPS measurements performed on the "as delivered" plates on three different positions showed an inhomogeneous distribution of Si-containing release agent on the CFRP surface (Table 2.3). The XPS results for the cleaned plates showed that pre-cleaning with IPA is effective in that the amount of release agent on the CFRP surface can be reduced to 0.5–1.4 at.% within the information volume of the investigation. This indicates the

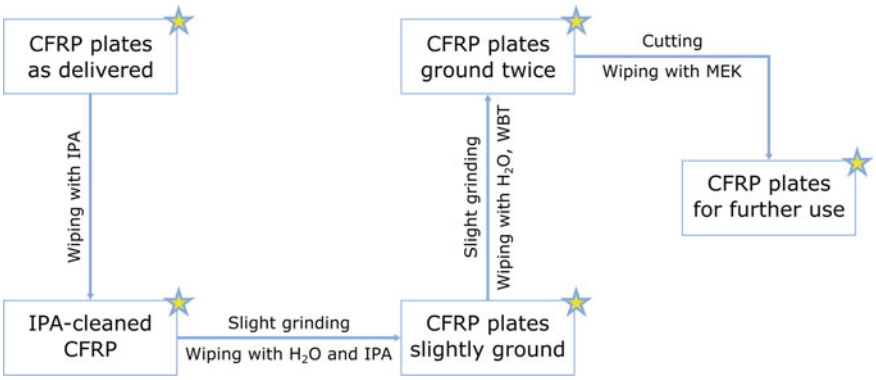


**Fig. 2.24** Process of the cleaning of as-received CFRP plates by moist wiping with water, isopropanol or methylethylketone soaked tissues and grinding with sandpaper

**Table 2.3** Surface Si concentrations (in at.%) from XPS investigations performed for the CFRP sample plates following the given cleaning steps with isopropanol (IPA)

| CFRP plates | Si (at.%) |
|---|---|
| CFRP "as delivered" sample plates | 5.3 ± 1.3 |
| CFRP sample plates after IPA cleaning | 0.9 ± 0.5 |
| CFRP sample plates after IPA cleaning and slight grinding | 0.3 ± 0.2 |
| CFRP sample plates after IPA cleaning and two slight grinding steps with cleaning in between | 0.1 ± 0.04 |

amount of dehesive material that can easily be removed by a subsequent abrasive grinding step without significant smudging.
2. Slight grinding of the surfaces to remove residual release agent that had penetrated or was incorporated into the topmost resin layers, and afterward wiping with demineralized $H_2O$ and IPA to remove the dust from the grinding, which comprised the inhering residual silicone. Further XPS measurements showed that a small amount of silicone remained on the surface (Table 2.3).
3. A second slight grinding step followed by wiping off the dust with demineralized water and IPA. On these samples, XPS measurements showed a very clean surface Table 2.3.

After the cleaning steps, the sample plates were wiped with methylethylketone (MEK) soaked tissues prior to performing the intentional contamination (corresponding to the respective scenario) and the subsequent adhesive bonding.

For the release agent contamination scenario (RA), the first and last dip-coating samples for each dip-coating solution (labeled RA-1, RA-2, or RA-3) were used for the XPS measurements; these were conducted on three positions (top, middle, bottom) on each sample. The results are shown in Table 2.4.

Based on these results, samples with the final concentrations of Si on the CFRP surfaces were obtained, as shown in Table 2.5.

For the production fingerprint contamination, three samples with each FP concentration were prepared for the XPS measurements. The results are shown in Table 2.6.

Based on these results, the concentrations of Na and Cl on the CFRP surfaces for each contamination level could be determined, as described in Table 2.7.

For the repair fingerprint scenario (FP), the locally applied Skydrol has the tendency to spread over the surrounding surface, thus no clear fingerprints can be observed after some time. Systematic XPS measurements were not conducted for this contamination scenario since most of the oil evaporates in the vacuum of the analysis chamber.

Since the de-icer contains potassium formate, the potassium content on the surface is taken as a measure for the degree of de-icer contamination. Dip-coating of the final de-icer contaminated samples was performed using solutions of 2, 7, and 10% de-icer in demineralized water. The samples for XPS control were dip-coated together with these samples. The XPS results are shown in Table 2.8.

Based on these results, the final concentrations of potassium on the CFRP surfaces for each contamination scenario were determined (Table 2.9).

**Table 2.4** XPS results (indicating the surface concentrations of the main elements [in at.%] as obtained) for CFRP plates after dip-coating in Frekote solutions (following RA-1, RA-2, RA-3) with different concentrations

| Samples | C (at%) | O (at%) | N (at%) | Si (at%) | S (at%) | Na (at%) |
|---|---|---|---|---|---|---|
| RA-1 start, top | 69.7 | 19.6 | 6.8 | 2.6 | 1.2 | <0.1 |
| RA-1 start, middle | 67.1 | 22.2 | 5.2 | 3.6 | 1.4 | <0.1 |
| RA-1 start, bottom | 66.6 | 20.5 | 6.6 | 5.1 | 0.8 | <0.1 |
| RA-1 end, top | 70.0 | 19.2 | 6.9 | 2.5 | 0.9 | 0.2 |
| RA-1 end, middle | 70.4 | 18.6 | 7.1 | 2.6 | 1.1 | 0.1 |
| RA-1 end, bottom | 69.9 | 19.1 | 7.1 | 2.6 | 1.0 | 0.2 |
| RA-2 start, top | 67.3 | 20.9 | 6.5 | 4.3 | 1.1 | <0.1 |
| RA-2 start, middle | 64.9 | 22.1 | 6.1 | 5.6 | 1.0 | <0.1 |
| RA-2 start, bottom | 66.1 | 20.8 | 6.9 | 5.2 | 0.7 | <0.1 |
| RA-2 end, top | 68.4 | 19.2 | 7.2 | 4.2 | 0.8 | <0.1 |
| RA-2 end, middle | 65.4 | 21.3 | 6.6 | 5.2 | 0.9 | 0.1 |
| RA-2 end, bottom | 65.2 | 21.1 | 6.5 | 5.9 | 0.7 | 0.3 |
| RA-3 start, top | 66.0 | 20.4 | 6.9 | 5.8 | 0.7 | <0.1 |
| RA-3 start, middle | 63.2 | 23.1 | 5.7 | 6.4 | 0.9 | 0.3 |
| RA-3 start, bottom | 64.8 | 21.0 | 6.6 | 6.6 | 0.6 | <0.1 |
| RA-3 end, top | 65.3 | 22.2 | 5.0 | 6.3 | 1.1 | <0.1 |
| RA-3 end, middle | 65.4 | 21.0 | 6.5 | 6.1 | 0.7 | <0.1 |
| RA-3 end, bottom | 64.5 | 23.0 | 4.8 | 6.2 | 1.1 | <0.1 |

**Table 2.5** Average concentration of Si on CFRP surfaces (obtained by XPS) for the RA contamination scenario

| Scenario | Si (at.%) |
|---|---|
| RA-1 | $3.2 \pm 1.0$ |
| RA-2 | $5.1 \pm 0.7$ |
| RA-3 | $6.2 \pm 0.3$ |

**Table 2.6** XPS results indicating the surface concentrations (main elements) of three CFRP plates contaminated with different (salty) solutions (FP-1, FP-2, FP-3) applied as a fingerprint

| Samples | C (at%) | O (at%) | N (at%) | Si (at%) | Zn (at%) | Cl (at%) | S (at%) | Na (at%) |
|---|---|---|---|---|---|---|---|---|
| FP-1, sample 1 | 74.6 | 15.3 | 8.5 | 0.2 | 0.1 | 0.4 | 0.6 | 0.2 |
| FP-1, sample 2 | 74.5 | 16.6 | 6.3 | 0.2 | 0.2 | 0.8 | 1.0 | 0.3 |
| FP-1, sample 3 | 74.7 | 16.6 | 6.8 | 0.2 | <0.1 | 0.3 | 1.0 | 0.2 |
| FP-2, sample 1 | 74.0 | 15.0 | 8.8 | <0.1 | <0.1 | 0.9 | 0.7 | 0.5 |
| FP-2, sample 2 | 73.2 | 16.8 | 7.3 | <0.1 | <0.1 | 0.9 | 1.0 | 0.6 |
| FP-2, sample 3 | 74.5 | 17.2 | 5.2 | 0.2 | <0.1 | 0.9 | 1.4 | 0.5 |
| FP-3, sample 1 | 73.8 | 16.0 | 7.5 | 0.1 | - | 0.9 | 1.1 | 0.6 |
| FP-3, sample 2 | 73.3 | 15.3 | 8.5 | 0.1 | <0.1 | 1.2 | 0.8 | 0.8 |
| FP-3, sample 3 | 73.3 | 16.1 | 7.4 | 0.1 | - | 1.2 | 1.1 | 0.8 |

**Table 2.7** Selected average surface concentrations (from the XPS results) of CFRP samples treated with differently concentrated solutions (FP-1, FP-2, and FP-3) applied as a fingerprint

| Scenario | Na (at.%) | Cl (at.%) |
|---|---|---|
| P-FP-1 | $0.2 \pm 0.1$ | $0.5 \pm 0.3$ |
| P-FP-2 | $0.5 \pm 0.1$ | $0.9 \pm 0.0$ |
| P-FP-3 | $0.7 \pm 0.1$ | $1.1 \pm 0.2$ |

## *2.6.2 Ultrasound Results*

### 2.6.2.1 Coupons

In this section, the results from the two different phased array probes used are presented, depending on the highlighted feature. Various types of defects were observed over the complete set of samples; these can be grouped into the three categories detailed below. The first one contains observations of a minor defect due to manufacturing; the second one comprises slight deviations from the reference; and the third one is the category of obvious defects with possible consequences for the ENDT measurements. Illustrations are given in the following sub-sections.

**Table 2.8** Final XPS results indicating the surface concentrations at distinct positions (pos.) for CFRP samples contacted with different de-icer dip-coating concentrations (DI1, DI2, DI3)

| Samples | C (at%) | O (at%) | K (at%) | S (at%) | Si (at%) | Cl (at%) | N (at%) | Na (at%) |
|---|---|---|---|---|---|---|---|---|
| DI-1 sample 1, pos. 1 | 58.4 | 28.5 | 8.9 | 0.8 | 0.3 | 0.3 | 2.6 | 0.3 |
| DI-1 sample 1, pos. 2 | 62.5 | 25.9 | 6.2 | 0.9 | 0.3 | 0.3 | 3.7 | 0.2 |
| DI-1 sample 1, pos. 3 | 64.1 | 25.7 | 4.3 | 0.9 | 0.3 | 0.3 | 4.3 | <0.1 |
| DI-1 sample 2, pos. 1 | 61.9 | 26.2 | 8.4 | 1.0 | <0.1 | 0.5 | 1.8 | 0.1 |
| DI-1 sample 2, pos. 2 | 65.0 | 24.3 | 5.2 | 0.9 | <0.1 | 0.2 | 4.2 | <0.1 |
| DI-1 sample 2, pos. 3 | 63.5 | 25.0 | 5.6 | 0.6 | <0.1 | 0.2 | 4.7 | <0.1 |
| DI-2 sample 1, pos. 1 | 55.7 | 30.5 | 11.0 | 0.6 | 1.0 | 0.2 | 0.8 | 0.2 |
| DI-2 sample 1, pos. 2 | 51.8 | 32.9 | 12.8 | 0.5 | 0.6 | 0.2 | 0.8 | 0.3 |
| DI-2 sample 1, pos. 3 | 51.5 | 31.8 | 13.8 | 0.6 | 1.0 | 0.2 | 0.9 | 0.2 |
| DI-2 sample 2, pos. 1 | 63.8 | 24.9 | 7.4 | 1.0 | <0.1 | 0.2 | 2.6 | 0.1 |
| DI-2 sample 2, pos. 2 | 62.6 | 24.4 | 10.2 | 0.6 | 0.3 | 0.2 | 1.5 | 0.1 |
| DI-2 sample 2, pos. 3 | 63.9 | 23.3 | 10.0 | 0.6 | 0.4 | 0.2 | 1.5 | 0.2 |
| DI-3 sample 1, pos. 1 | 52.3 | 31.9 | 13.0 | 0.4 | 0.6 | 0.2 | 1.1 | 0.2 |
| DI-3 sample 1, pos. 2 | 55.2 | 30.5 | 11.2 | 0.6 | 1.1 | 0.1 | 1.1 | <0.1 |
| DI-3 sample 1, pos. 3 | 55.7 | 29.2 | 11.8 | 0.6 | 0.9 | 0.2 | 1.3 | 0.3 |
| DI-3 sample 2, pos. 1 | 57.5 | 28.7 | 11.9 | 0.5 | 0.4 | 0.2 | 0.4 | 0.3 |
| DI-3 sample 2, pos. 2 | 57.3 | 29.6 | 9.9 | 0.9 | 0.2 | 0.1 | 1.7 | 0.2 |
| DI-3 sample 2, pos. 3 | 53.8 | 29.3 | 14.0 | 0.6 | 0.6 | 0.1 | 0.8 | 0.2 |

**Table 2.9** Average concentration of potassium on CFRP surfaces for the DI contamination scenario

| Scenario | K (at.%) |
|---|---|
| DI1 | 6.4 ± 1.8 |
| DI2 | 10.9 ± 2.3 |
| DI3 | 12.0 ± 1.4 |

*First category of defects: Minor defects due to sample manufacturing*

The defect types within this category can be itemized into three groups. These are most likely due to the sample manufacture and are expected to have no impact or a low impact on the ENDT measurements:

- Bending of the bonded specimens (Fig. 2.25a). This defect type was particularly observed for the repair reference samples as well as some of the samples within the TD scenario. The observed curvature is evidenced on the FWE amplitude cartography with the 5 MHz probe, as shown in Fig. 2.25a. In fact, a phased array measurement was only possible using the SAUL option to partially compensate for the curvature and the induced misalignment of the probe with the sample along its

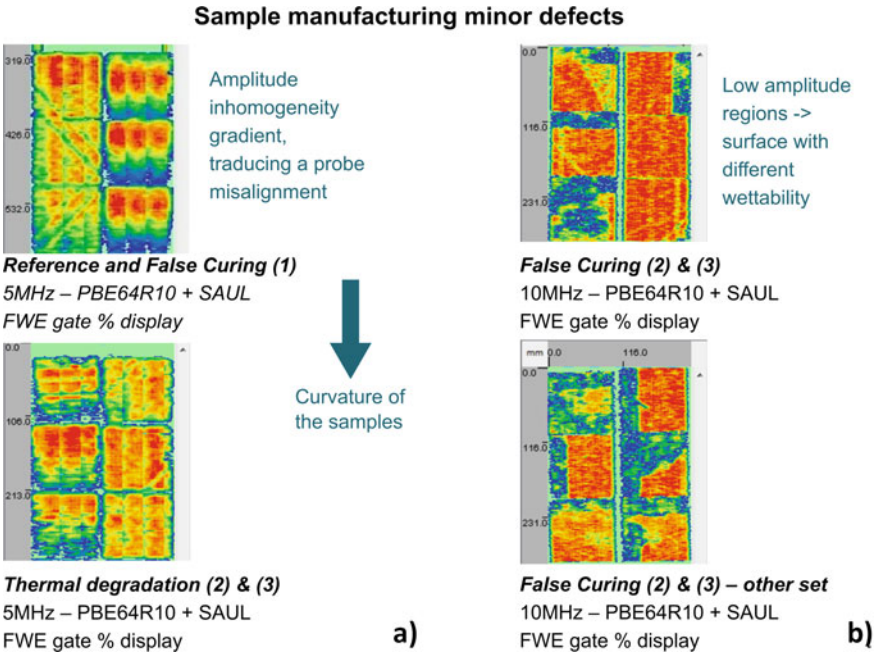


**Fig. 2.25** Overview of the minor manufacturing defects observed during the ultrasonic inspection of CFRP specimens, with typical examples of **a** the bending of samples and **b** the surface quality problem

length. However, even if this defect has an effect on the ultrasonic measurements, it should have no consequences for the ENDT investigations.

- Bad quality of the composite surface (Fig. 2.25b). This defect type was evidenced using the 10 MHz probe on the FWE amplitude cartographies. Indeed, the cylindrical focusing of the probe increases the sensitivity to such surface defects. These were generally located on edges and were probably due to marks left by the adhesive tape used during the manufacture. In these areas, wettability with the ultrasound coupling medium is probably different, thus leading to low amplitude regions. In other rare cases, the wall surface was covered, probably due to resin leakage.

*Second category of defects: Minor deviation from the reference, potentially due to contamination*

Other sample inspection results presented a significant deviation from the reference measurements, albeit without clear evidence of a defect (Fig. 2.26). Specifically, in case of CFRP samples from the P-MO and P-FP scenarios, the bond echo amplitude is of approximately the same order of magnitude as the BWE, whereby this is not the case for the reference and other contaminated samples (as shown by the release agent samples in Fig. 2.26). This observation could be due to higher bond impedance or lower back composite skin impedance. In other words, it could be a sign of bond alteration or composite alteration (especially in the case of moisture). This was evidenced using g+gate TOF cartography, which displays the position of

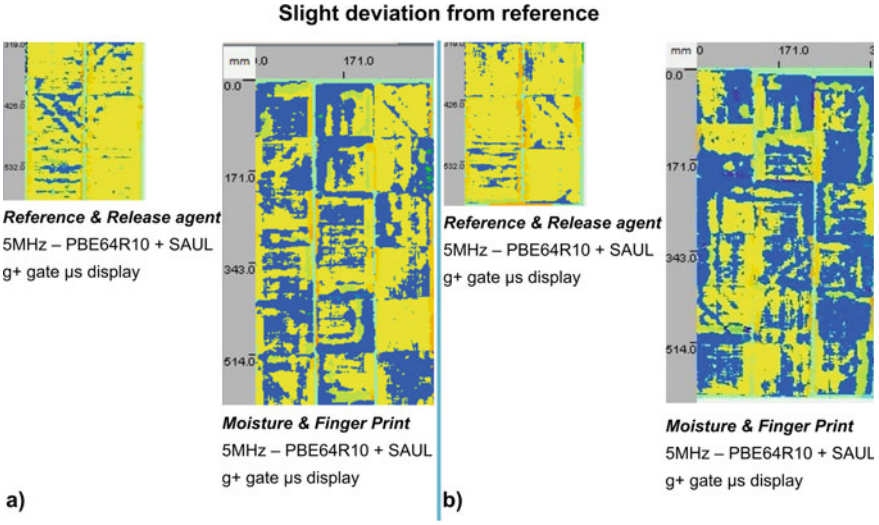


**Fig. 2.26** Example of ultrasonic inspection results for CFRP specimens showing a slight deviation from the reference, taking the "g+" gate display for the reference and release agent scenario or for the moisture and fingerprint combined contamination scenario; **a** first sample set as an example and **b** second sample set as an example

the maximum echo in the sample thickness. Referring to the color coding used for displaying the results of the ultrasound investigations, blue corresponds to the bond echo, and yellow to the BWE. A mix between blue and yellow means that the echoes are of approximately the same order of magnitude, while only yellow means that BWE dominates. Two examples are given in Fig. 2.26a for the first set of samples, while Fig. 2.26b shows the second set. This effect is so far neither well defined nor explained, but it might be due to contamination. However, this does not prevent these samples from being considered as weak bonds.

*Third category of defects: Obvious defects due to "contamination"*

Finally, more sizeable and obvious defects with a potentially highly detrimental effect on the future ENDT measurements were observed, namely delamination and disbonding. CFRP specimens having undergone faulty curing or thermally degraded samples are the main concerns here. In these cases, the state of the joint of the samples cannot be considered as presenting as a weak bond but rather as a bond with defects. All the observed defects are presented in Figs. 2.27 and 2.28.

In the FC-1 samples (Fig. 2.27), the regions showing the effects of debonding are evidenced in the middle of each plate. A defect signature is visible in the bond amplitude and TOF cartographies. The highest amplitude and a small shift in TOF, respectively, show debonding with a high contrast. Consequently, defects are also visible on the BWE amplitude gate, with a low amplitude region, and in the "g+" TOF cartography. The sizes of the debonding regions vary depending on the samples but are usually above 1 cm and up to 5 cm. These debondings are located in the middle of the bonded coupons and, thus, they could have a significant impact on the ENDT measurements. Note that some small debonding spots (smaller than 1 cm) are also observed in some of the FC-2 samples. These defects were probably induced by the way the samples were manufactured.

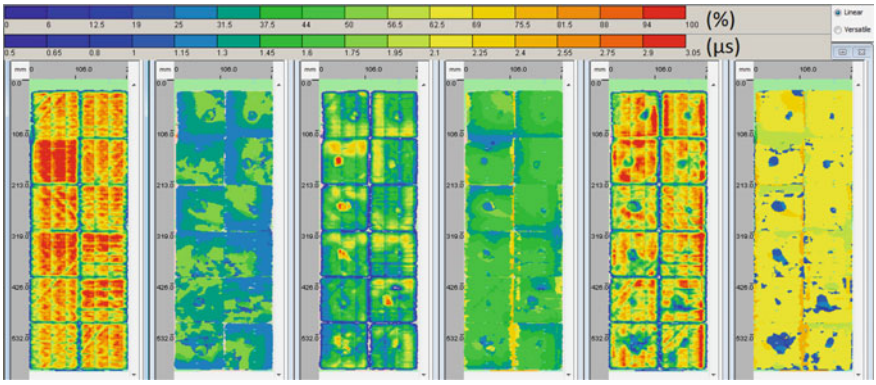


**Fig. 2.27** Results of the ultrasound investigations for samples within the FC-1 scenario—observation of disbonding in all the samples with defects showing a size range of 1–5 cm

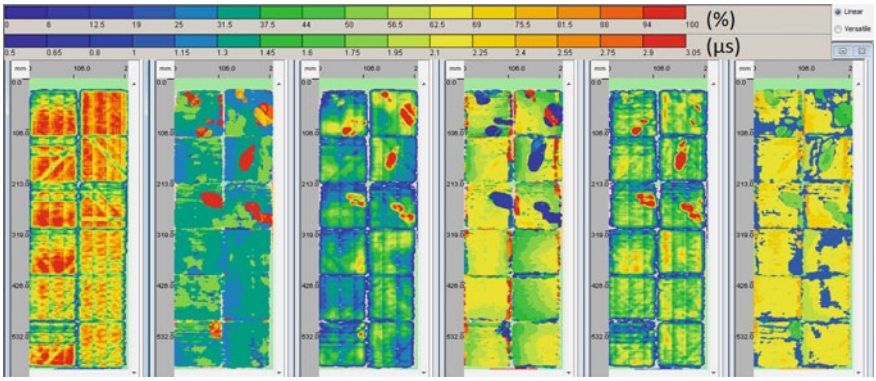


**Fig. 2.28** Results of the ultrasound investigations for all samples within the TD-3 scenario—observation of delamination, in some samples with a size in the range of 2–5 cm

For the TD-3 samples, important delaminations were highlighted by ultrasonic inspection (Fig. 2.28), however not for all samples. The delaminations are evidenced by all the gates because they are located on the first composite skin, i.e. the one that has been thermally affected. This is confirmed by the "g+" TOF cartography (cf. light green color coding in the figure of Table 2.10). Therefore, the defect signature enters the bond gate and has consequences on all the other gates. Because of their considerable size (several centimeters) these delaminations could have a strong influence on results obtained using ENDT techniques.

The most profound investigations were achieved using a post-treatment tool. In this work, the NDTKit analysis software was used to obtain the ultrasound data for the CFRP samples (the commercial version of this software is named Ultis), whereby "defect detection" was enabled to size some of the defects. An example of a case of faulty curing is presented in Table 2.10, together with the main characteristics typical for disbonding and described according to the parameters of position on the plate, surface, outline surface, length, and mean value (for TOF). We note that the origin of the defect is at the top left-hand corner of each plate.

### 2.6.2.2 Combined Contamination Coupons

Multi-contaminated samples were also investigated using the same methodology and the same instrument settings as described above. Essentially, the same kinds of defects were observed for these samples, which is as expected since their manufacturing and contamination procedures were the same. Some examples are given in Fig. 2.29, and are these are further detailed below.

Minor defects were also observed; in this case, they are attributed to clamp marks, as shown in Fig. 2.29a. These are located on the edges and occur during the sample manufacture (probably while stabilizing the plate for bonding). On the ultrasound data acquisitions, they are visible on the bond amplitude C-scan as well as on the

**Table 2.10** Example of an ultrasound-based defect detection result for CFRP coupons prepared within the faulty curing scenario, indicating the position in the plate, surface, outline surface, length, and mean value (for TOF)

| Defect detection | Names (centers) | Surface ($mm^2$) | Outline ($mm^2$) | Length (mm) | Mean ($\mu s$) |
|---|---|---|---|---|---|
| 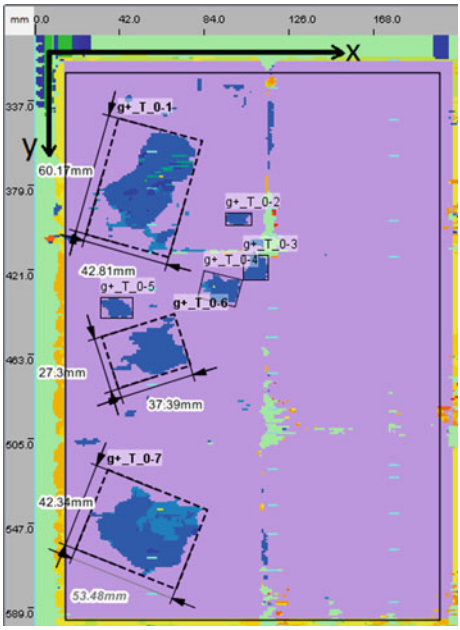 | g+_T_0-1 (X = 43, Y = 62) | 1328.0 | 2575.6 | 60.2 | 1.08 |
| | g+_T_0-2 (X = 92, Y = 81) | 57.0 | 78.0 | 13.0 | 1.08 |
| | g+_T_0-3 (X = 98, Y = 7) | 115.0 | 144.0 | 12.0 | 1.09 |
| | g+_T_0-4 (X = 80, Y = 20) | 174.0 | 260.2 | 19.2 | 1.12 |
| | g+_T_0-5 (X = 28, Y = 27) | 108.0 | 160.0 | 16.0 | 1.08 |
| | g+_T_0-6 (X = 49, Y = 49) | 517.0 | 1020.9 | 37.4 | 1.07 |
| | g+_T_0-7 (X = 44, Y = 44) | 1350.0 | 2264.3 | 53.5 | 1.12 |

FWE gate. Indeed, this type of defect is often associated with a bond material leakage on the composite surface (due to bond creep). Therefore, the composite surface is also modified. Note that these areas are also often associated with a bond thickness reduction. Moreover, slight deviations from the reference can also be evidenced in the case of the "release agent+fingerprint" scenario. The effect is in this case probably the same as the one explained in the previous section, namely that a higher bond impedance may have been induced by the contamination. Since this effect was not observed when considering the release agent contamination alone, it might mean that additionally applying the fingerprint is causal for this signature in the combined contamination samples.

### 2.6.2.3 Curved Specimens

Finally, the curved specimens were tested. Compared to inspecting the flat samples using ultrasound, these inspections are more challenging because of the geometry of the part. The echo entry face reverberates almost all the incoming energy in a divergent beam. Therefore, it is very hard to inspect such a type of geometry with

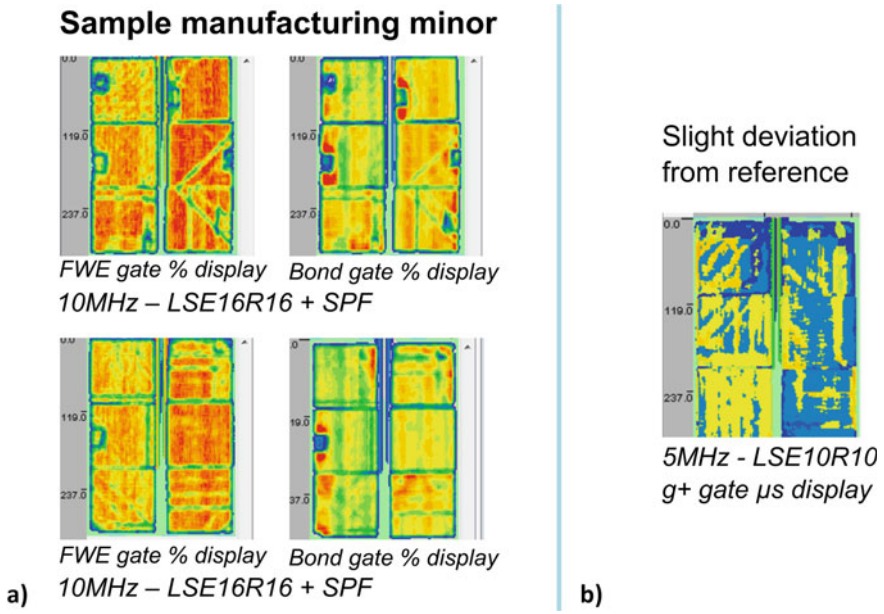


**Fig. 2.29** Overview of the defects observed by ultrasound investigations of CFRP samples from the combined contamination scenarios, especially the scenario "release agent+finger print"; **a** minor manufacturing defect and **b** minor deviation from reference

a regular phased array setting. An example of an inspection result when using a conventional linear scanning configuration is shown in Fig. 2.30. Only one small part of the sample appears in the cartography for the curved specimen. The thus inspected region corresponds to the place where the sample surface is oriented closest to parallel to the probe, plausibly in the middle of the curved specimen. Everywhere else, no echo was measured, which is attributed to the fact that all the waves were reflected away from the probe.

To solve this issue, the SAUL algorithm was used. The idea is to first describe the surface geometry by using the ultrasonic phased array like a radar, whereby the

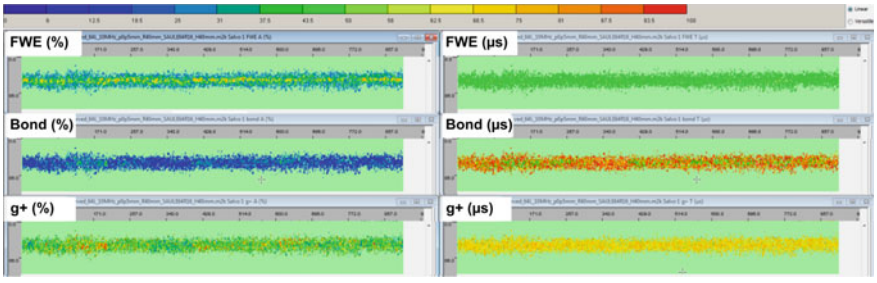


**Fig. 2.30** Inspection results for a curved CFRP when using a linear scanning configuration

distance to each element of the probe is detected. Subsequently, the delay laws are calculated to generate an ultrasonic wavefront that will fit the sample geometry. In Fig. 2.31, an example based on a CIVA numerical simulation is presented in order to explain the principle. The elements on the edges are shot first, while those in the middle are shot in the last position.

The curved CFRP sample inspections when applying SAUL are presented in Fig. 2.32. The results show that the specific algorithm helps to complete the inspection. We did not notice any lack of data acquisition in any region of the specimen, and the echo-wall "ew" amplitude was more or less homogeneous. Inspections were thus possible thanks to SAUL, and the obtained signal could be used to make a statement

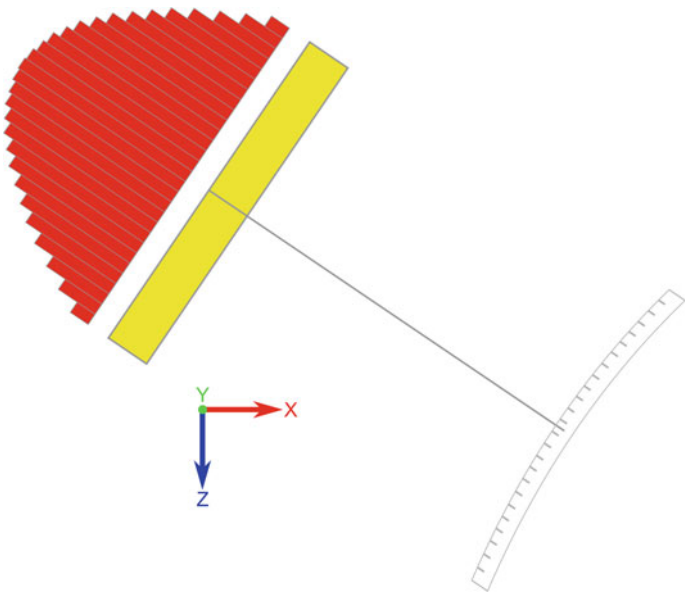


**Fig. 2.31** Sketch showing an example of a SAUL (surface adaptative ultrasonic laws) calculation applying CIVA software

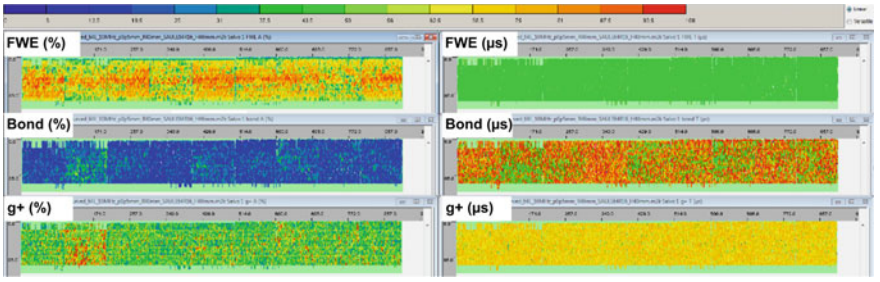


**Fig. 2.32** Ultrasound inspection results for a curved CFRP specimen using a SAUL configuration

about the material quality, which appears to be very poor. Indeed, the amplitude of the BWE turned out to be very low. The TCG had to be significantly increased in order to receive a signal from the back wall. This necessary increase in the gain is an indication of strong attenuation, probably due to a high porosity content. Thus, it is difficult to give a clear statement on the bond quality, since the quality of the composite adherends might be the main issue.

### *2.6.3 Fracture Toughness Results*

As presented in the previous sections, pre-bond contamination was systematically arranged and intentionally performed on CFRP adherends, and the adherend surfaces as well as the resulting CFRP bonded joints were then characterized by means of reference laboratory non-destructive testing (NDT) methods. Subsequently, the results from the destructive testing regarding the respective joint strength are reported and the effects of the carefully adjusted deviation from the qualified bonding process are evaluated based on the observed joint strength and fracture pattern, which are a common design quantity constituting a joint specification. Using the terminology introduced in Chap. 1 for the concept of quality assessment in adhesive bonding suggested in this book, in the aircraft production this strength is considered a design-relevant operands feature.

#### 2.6.3.1 Mode-I Testing

The average $G_{IC}$ values of the specimens manufactured within the production and repair scenarios are presented and compared in the compendious histograms in Fig. 2.33 and Fig. 2.34, respectively. The reference category samples denoted as

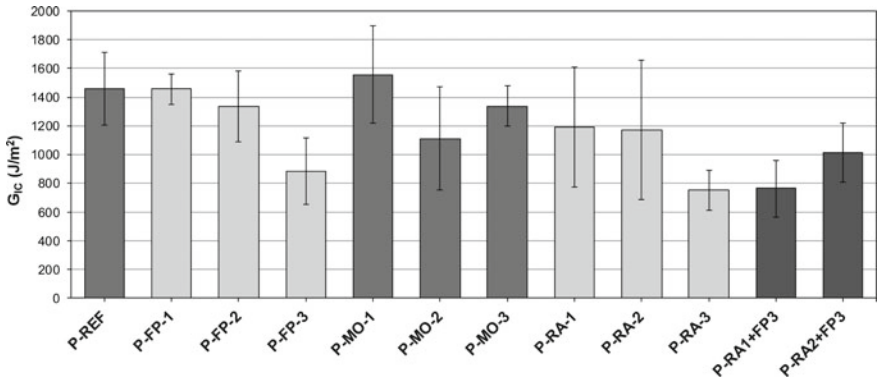


**Fig. 2.33** The average $G_{IC}$ values for bonded CFRP joints in a comparison of the production (P) scenarios

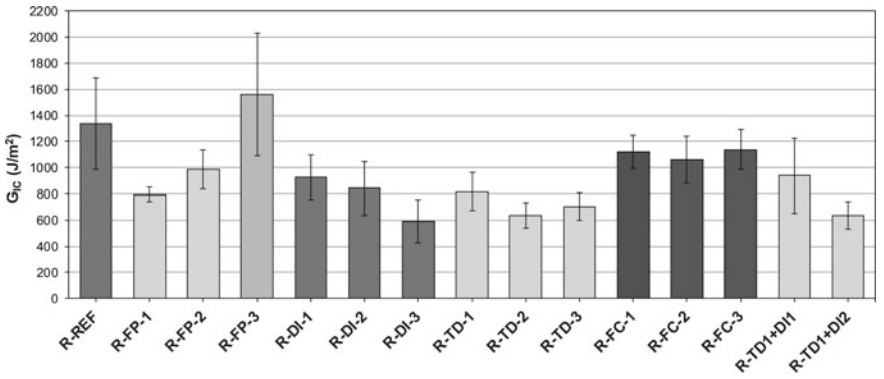


**Fig. 2.34** The average $G_{IC}$ values for bonded CFRP joints in a comparison of the repair (R) scenarios

P-REF and R-REF exhibited the highest fracture toughness values while the experimental results indicate a mainly negative effect of the contamination introduced in the respective scenario.

The characterization of the failure mode observed for the respective fracture surfaces showed that adhesive failure was the dominant failure for all the production-related scenarios regardless of the contamination case or level. The adhesive fracture occurred for both the intentionally contaminated substrates in the production and the repair scenarios, but in a different way for each specimen (the pattern and amount of separated adhesive differ), contributing to the large scatter effect observed in the $G_{IC}$ values. In the repair reference samples, a mixed-mode failure was observed (Fig. 2.35), with the dominant failure being a light fiber tear failure, at 50%.

When investigating the joints manufactured following the production fingerprint contamination scenario (P-FP), the respective observed $G_{IC}$ values decreased as the level of contamination by the artificial hand perspiration solution increased. Specifically, for the joints prepared following the P-FP-1 deviation from the qualified production process used for the set of reference joints, the average $G_{IC}$ value was the same as obtained for the reference joints. This indicates that a low concentration level of the FP contamination does not affect the performance of the bond. For P-FP-2, the average $G_{IC}$ decreased by 8%, while for the high contamination level P-FP-3 the $G_{IC}$ fracture toughness of the joints decreased significantly, by 39%. These findings show the detrimental effect of FP contamination on bond performance.

Regarding moisture contamination, for the joints produced following MO-1, the average $G_{IC}$ values show an almost 7% increase compared to the reference category. Considering the observed mixed-fracture pattern, such a finding might be attributed to a modification of the CFRP material by a moderate water uptake, which causes plasticization of the polymeric matrix due to dispersing water molecules. However, in the MO-2 production scenario, the average $G_{IC}$ value was reduced by 24%, and in the MO-3 by 8% as compared to the reference value. Considering the large standard deviation observed, especially for the MO-2 samples, extrapolating a straightforward

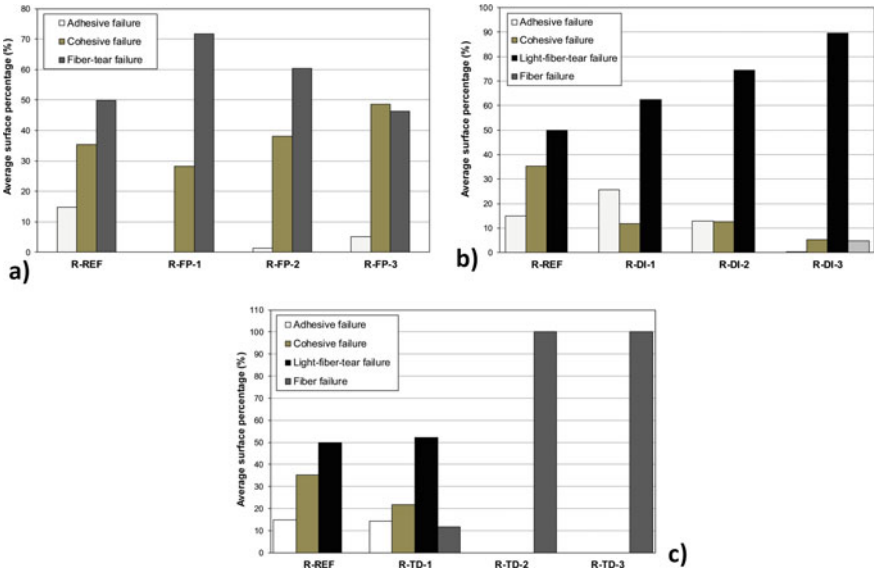


**Fig. 2.35** Average percentages of fracture modes obtained after mode-I testing of the joints manufactured within the repair scenarios **a** R-FP, **b** R-DI, and **c** R-TD

structure-property relationship regarding the effect of a medium or high level of moisture contamination on bondline integrity is hindered. In any case, observing a changed average value or a higher standard deviation for the findings related to the design quantity fracture toughness indicates that moist CFRP adherends should be considered an issue for the quality assessment of the resulting bonded joints.

Evaluating the effects of applying even small amounts of release agent to CFRP adherend surfaces within the RA scenario indicates that there are substantial effects on the observed fracture toughness for the thus produced adhesive joints. When the production follows the low-level contamination RA-1 scenario, the average $G_{IC}$ values show an almost 18% reduction compared to the reference category, and for RA-2 the average $G_{IC}$ is reduced comparatively clearly by 20%. The large scatter of the $G_{IC}$ values of the RA-1 and RA-2 samples denotes that there is no statistically significant difference between the effects of the RA-1 and RA-2 contaminations; however, the negative effect of the release agent contamination on the fracture toughness of the bonded joint is evident when compared to the joints produced following the qualified process. For RA-3 the fracture toughness of the joints degrades significantly, by 43%, demonstrating the detrimental effect of the release agent on bond performance. Moreover, the mixed-fracture pattern indicating a weak bond is observed in this case, in clear contrast to the fracture pattern of the joints produced following the P-REF scenario.

Finally, the effects of following a combined contamination scenario with release agent and fingerprint during the production process were investigated with respect to the fracture toughness. The results indicate a significant reduction of the $G_{IC}$ value

of the bonded joints that is greater than the reduction caused by each contaminant separately, indicating that the combination of contaminations may be more detrimental to the composite bonded joints' performance. Specifically, the $G_{IC}$ values in the RA1+FP3 and RA2+FP3 scenarios decreased by 48% and 30%, respectively, compared to the reference category values. It is worth mentioning that a consecutive combination of the contamination RA2+FP3, i.e. first a contamination as for RA2 and then as for FP3, led to a smaller $G_{IC}$ reduction than the nominally lower contamination level of RA1+FP3. This finding may indicate that the interaction of a high RA level with FP3 affects the fracture toughness of the bondline less than the interaction of a low RA level with FP3. With both the release agent and the artificial hand perspiration solution resulting in filmy deposits on the CFRP surface upon drying, the supposed interaction between the contaminations is attributed to the effect that the hydrophobic and barely water-soluble release agent film exercises on the transfer and/or film formation of the aqueous solution, which finally dries on top of it.

Subsequently, we discuss the $G_{IC}$ findings displayed in Fig. 2.34, meaning that the focus will be on the mechanical characteristics of joints manufactured according to a repair scenario. The evaluation of the, respectively, obtained fracture pattern is presented in Fig. 2.35. In contrast to the deleterious effect of films from the artificial hand perspiration solution observed for joints prepared within the P-FP category, for the R-FP scenario the contamination with a Skydrol fingerprint seems to have a different scaling effect on the mechanical performance of the joint. We refer to the finding that although R-FP contamination degrades the mode-I fracture toughness of the joint, a reduced decrease in the $G_{IC}$ values was surprisingly observed for samples provided with higher contamination levels. This phenomenon was also supported by the failure mode presented in these samples, whereby an increasing cohesive failure mode was observed (Fig. 2.35a). While a discussion based on additional findings from the surface characterization will not be initiated here, intuitively such a trend would hardly be expected if—in an analogy to the RA scenario—an increasingly thicker inert film with a low cohesion were formed on CFRP surfaces upon contact with increasingly concentrated Skydrol formulations.

Returning to Fig. 2.34 and moving on to the contamination scenario based on depositing residues from a drying aqueous solution of de-icing agents onto CFRP adherends, the fracture toughness results indicate a detrimental effect of dried de-icer fluid on the bond performance as $G_{IC}$ is reduced for all three contamination levels (up to 56% for the DI3 contamination level). The large scatter of $G_{IC}$ values is attributed to the complexity of the adhesion mechanisms and the failure mechanisms (unstable crack propagation, varying failure modes) and possibly to a non-uniformity of the contamination [1, 17]. Considering the respective fracture patterns, it was observed that when increasing the contamination level there is an increase in the percentage of areas exhibiting LFT failure (Fig. 2.35b), which is a clear sign that contact with de-icing fluid degrades the tensile strength of the matrix.

Concerning the TD scenarios, thermal impact and degradation constitute an external influence on a well-characterized material rather than a contamination, e.g. by deposited substances. High temperatures can cause local overheating, damage the CFRP resin and even affect the fiber/matrix interaction due to the differences in

thermal elongation between matrix and fiber. The average $G_{IC}$ was reduced by 39%, 53%, and 58% for the joints prepared following the TD-1, TD-2, and TD-3 cases, respectively, as compared to the reference category. However, the $G_{IC}$ value obtained following an exposure of the adherends to the higher degradation temperature (TD-3) was not significantly lower than that observed after an exposure to the temperature of the TD-2 scenario. Although the opposite might be expected, it should be noted here that in some cases [17, 26, 27] it has been reported that high temperatures can cause oxidation, especially at the surface of the resin, which, due to the formation of carbonyl surface groups, may even improve adhesion. This aspect is expected to be less relevant when comparing the effects of the TD-2 and TD-3 scenarios because the thermo-oxidatively affected CFRP surface region had been removed in a grinding process prior to the bonding step. In any case, thermally affected CFRP adherends are clearly an issue for the quality assessment of adhesively bonded joints. Based on the fracture pattern evaluation, the dominant failure was the LTF failure and its percentage increased as the temperature to which the CFRP adherends were exposed increased, with LTF portions reaching up to 100% of the fracture surface area for joints prepared following the TD-2 and TD-3 scenarios (Fig. 2.35c). This indicates that considerable damage was caused to the CFRP adherends due to thermal degradation.

When inspecting the $G_{IC}$ values of the joints with the faulty curing of the adhesive and comparing them with those obtained for the reference joints, it is evident that there was a degradation of 15–21%. Evidently, the non-proper curing of the adhesive in a joint can be very detrimental. Considering the rather large scatter between the fracture toughness values of the joints with the faulty curing of the adhesive, a significant distinction between the effects of the three contamination levels within the TD scenario was not found.

Finally, a contamination scenario that combined the thermal impact on the CFRP adherends and a deposit of dried de-icer was studied and a loss of the bond quality—mirrored by a lower fracture toughness—was observed. Specifically, the $G_{IC}$ values for samples of the combined scenarios R-TD1+DI1 and R-TD1+DI2 decreased by 30% and 52%, respectively, compared to the values observed for joints from the reference category. Especially for the higher level of combined contamination, i.e. TD1+DI2, the $G_{IC}$ reduction was greater than the reduction that each contamination scenario induced separately.

#### 2.6.3.2 Mode-II Testing

The average $G_{IIC}$ values of the samples prepared either following the qualified production and repair processes or after intentionally introducing process deviations during production or repair are presented and compared in the histograms displayed in Fig. 2.36 and Fig. 2.37, respectively. Subsequently, we will present and discuss our findings beginning with the tested as-bonded specimens and then regarding the effects of environmental aging for specimens that underwent a hygrothermal exposure prior to testing the mode-II fracture toughness.

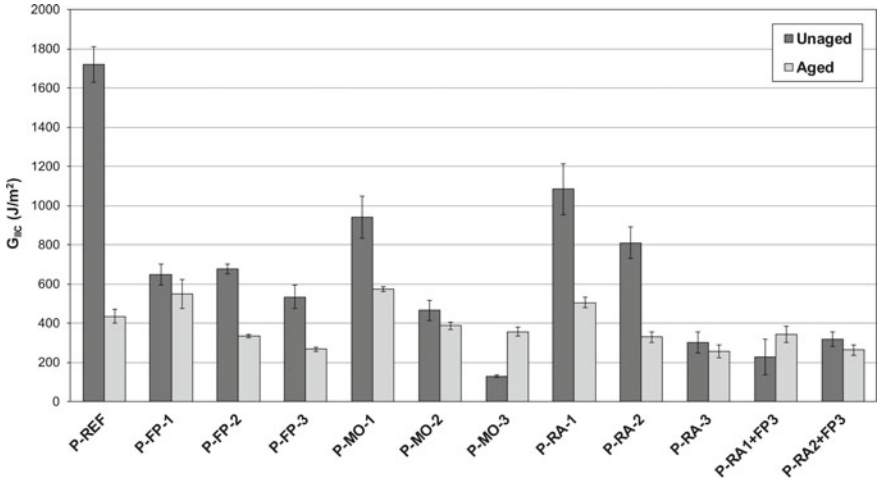


**Fig. 2.36** Comparison of the average $G_{IIC}$ values for bonded CFRP joints in the production scenarios before and after hygrothermal environmental aging

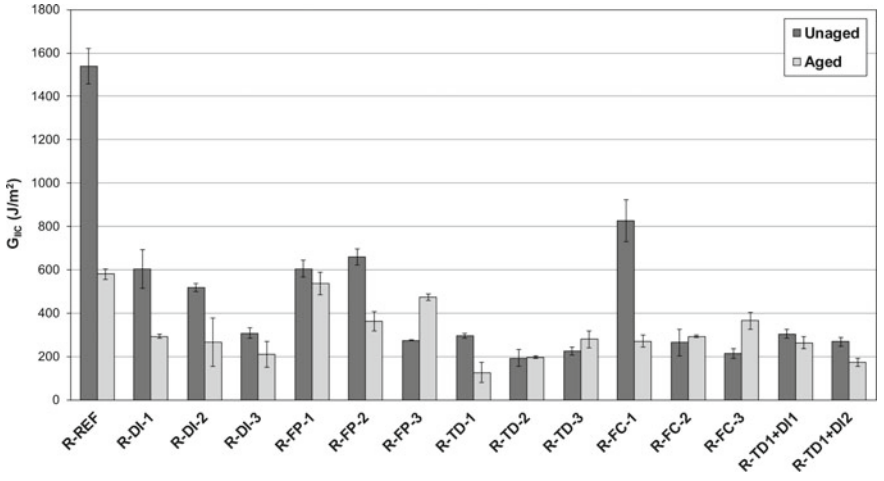


**Fig. 2.37** Comparison of the average $G_{IIC}$ values for bonded CFRP joints in the repair scenarios before and after hygrothermal environmental aging

As was observed for the average $G_{IC}$ values of the unaged specimens, the reference category samples exhibited the highest fracture toughness values, also with mode-II characterization. Implementing any of the previously described contamination scenarios during production or repair cases caused a decrease in the $G_{IIC}$ fracture toughness. The observed reduction, as compared to the values found for specimens from the P-REF and R-REF scenarios, respectively, was always greater than the decrease of the $G_{IC}$ values that was observed for the correspondingly prepared sample

sets. This finding indicates that the composite bond is more sensitive to contamination when loaded in mode-II (shear-induced crack propagation).

Starting with the $G_{IIC}$ tests of the unaged specimens, a detrimental impact of fingerprinting the CFRP adherend surface prior to bonding in the P-FP scenario was observed, also for the mode-II fracture toughness. When intentionally applying increased contamination levels for further sample sets within this scenario, this highly significant adverse effect was confirmed and a further reduction of the value of $G_{IIC}$ was found. Specifically, for both the P-FP-1 and the P-FP-2 cases a reduction of 61% was observed regarding the reference values, while for P-FP-3 the reduction reached 69%.

Clearly exceeding the effects observed the in mode-I test results, a profound impact of implementing the moisture contamination scenario for the adherends before bonding was revealed in the mode-II tests. An increase of the moisture concentration in the atmosphere applied during the storage of the adherends even caused a further $G_{IIC}$ reduction. Specifically, a reduction by 45% and 73% compared to the reference values was observed for the MO-1 and MO-2 cases, respectively, while for MO-3 the reduction reached 93%. These findings clearly reveal the detrimental effect of moisture absorption on CFRP adherends in the mode-II fracture toughness of the composite bonds. Moisture significantly lowers the quality of adhesion, and it also leads to a loss of performance in the CFRP material itself and, by extension, causes a loss of performance of the adhesive bond [1].

Concerning the mode-II investigations of specimens prepared from adherends intentionally contaminated by release agent, a detrimental effect on the fracture toughness was observed, which corresponds to the findings of the mode-I tests. Increasing the release agent concentration causes an even stronger $G_{IIC}$ reduction. Specifically, for RA-1 a reduction of the $G_{IIC}$ value by 37% was observed with regard to the reference values, while for RA-2 the corresponding value was 53% and for RA-3 the reduction reached 82%.

Finally, it was also observed that the combined contamination with release agent and fingerprint resulted in a pronounced reduction of the $G_{IIC}$ values for the sets of bonded joints. The decrease in fracture toughness was greater than the reduction caused by each contaminant separately, indicating that the effect of successively implementing two deposit-forming combination scenarios of contaminations may prove even more deleterious to the performance of bonded composite joints. Specifically, the $G_{IIC}$ values which were found after having applied the combined contamination RA1+FP3 and RA2+FP3 on the CFRP adherends during the manufacture of the joints were decreased by 87% and 82%, respectively, compared to the reference category values. As in the mode-I tests, the combination RA2+FP3 did not lead to a more distinct reduction of the $G_{IIC}$ value than the RA1+FP3 combination, in which a fingerprint was applied using the same diluted artificial hand perspiration solution but on top of a thinner release agent film.

The following will cover the results of $G_{IIC}$ tests performed with adhesive joints prepared following the distinct repair scenarios and presented in Fig. 2.37.

Intentionally applying runway de-icing fluid to the CFRP adherend surface before bonding has a similar impact on the mode-II fracture toughness of the resulting

joints as was observed in the mode-I fracture toughness testing. An increase of the de-icing fluid concentration used for the intentional CFRP surface contamination caused a further $G_{IIC}$ reduction. Specifically, when following the DI1 scenario a reduction of 56% was observed with regard to the reference values, while for DI2 the corresponding value was 62% and for DI3 the reduction reached 80%.

With respect to specimens from the R-FP contamination scenario, it was observed that the mode-II fracture toughness of the joints was drastically reduced. Specifically, applying R-FP-1 and R-FP-2 contamination levels caused a reduction of approximately 61%, while introducing R-FP-3 reduced the $G_{IIC}$ even further to 82% compared to the R-REF category. For all the tested joints a mixed-fracture image was found. Basically, this reduction in bond strength could be attributed to the fact that the FP contamination, with the hydraulic fluid transferred by fingerprinting, led to poor adhesion between the adhesive and the adherend, whereby kissing bonds were formed. However, the observed decrease in the fracture toughness as compared to the R-REF specimens and the obtained adhesive fracture image contrast with the findings for the joints based on correspondingly contaminated CFRP surfaces that were subjected to mode-1 testing and which, in the case of the R-FP-3 scenario, yielded increased $G_{IC}$ values as compared to the R-REF scenario as well as an adhesive fracture image. Therefore, we essentially highlight once again that, under mode-II loading, the composite bond is strikingly more sensitive with respect to the applied contamination than under mode-I loading.

Concerning joints prepared from adherends that had experienced thermal impact before being bonded within the TD scenario, an increase in the exposure temperature caused a further $G_{IIC}$ reduction. The average $G_{IIC}$ was reduced by 81%, 88%, and 86% for the TD-1, TD-2, and TD-3 cases, respectively, compared to the reference category. Again, the reduction for the TD-3 case was lower than for the TD-2 thermal degradation. The scatter hinders any clear distinctions to be made between the effects of applying the TD-2 and TD-3 scenarios on the adhesive composite bond integrity.

As in the mode-I tests, the mode-II tests revealed that the intentionally applied faulty curing of the adhesive within the repair scenario of CFRP joints can be detrimental to their resulting properties. Specifically, for the FC-1 scenario a reduction of 46% was observed with regard to the reference values, while for FC-2 and FC-3 the reduction was even more drastic, amounting to 83% and 86%, respectively.

Finally, applying the more complex repair scenario, which comprises a combination of thermal impact and degradation with an application of de-icing fluid contamination on the CFRP adherends before being bonded, results in a reduction of the $G_{IIC}$ value of the joints by 80% and 83% for the R-TD1+DI1 and R-TD1+DI2 cases, respectively. These effects are greater than the reduction of the $G_{IIC}$ value caused by each contaminant separately. These findings indicate that monitoring effects of successively applied contaminations is a task in the quality assessment of adherend surfaces as well as the performance of the resulting joints.

Aging Effect

Exposure to a hygrothermal environment is reported to be a critical issue regarding the durability of adhesively bonded joints whenever the applied demands are characterized by a combination of elevated temperature, moisture, exposure time, and mechanical loading [28]. For example, elevated parameter settings are applied in scenarios for highly accelerated life tests (HALT), which are used in the development of a joint design to quickly achieve indications of weak points [29] or to identify the functional operating limits exceeding the operational area defined by the product specifications [30]. Against this background and aiming at a comprehension of feasible deviations from the qualified bonding process in the development phase of an adhesive joint, we have decided to include such elevated hygrothermal parameter settings in the concept of the quality assessment for the manufacturing processes of CFRP composite adhesive joints. The effect of the externally applied environment in terms of moisture and temperature has been thoroughly investigated [31–33], essentially indicating a significant loss of the bond strength of joints subjected to aging, especially after reaching a moisture saturation in adhesive joints that were exposed to a high relative humidity or water immersion.

The combination of a pre-bond contamination of adhesive composite joints and after-bond exposure to hygrothermal aging leads to a drastic reduction of the $G_{IIC}$ (Figs. 2.36 and 2.37). In the majority of the investigated scenarios, the effect of applying the combination of pre-bond contamination and after-bond long-term hygrothermal aging to a set of bonded joints is more severe than the effect of applying either of the two scenarios separately.

The drastic reduction of the $G_{IIC}$ values ascertained when comparing the findings for sets of aged and unaged CFRP joints coincides with the fact that the onset of crack propagation was observed at the side of the specimen where the moisture concentration and thermal effect are higher [34]. Additionally, the crack propagation occurred near the adhesive region, and diffusion through the adhesive is regarded as the primary access route for moisture to enter a joint [35].

For example, the aging procedure resulted in a reduction in the mode-II fracture toughness of the R-REF samples by 62% compared to the unaged repair reference scenario (Fig. 2.37). Additionally, for all of the aged specimens of any of the applied contamination scenarios, the observed $G_{IIC}$ values of the aged samples were drastically reduced for all contamination levels compared to the respective unaged reference REF category. Surprisingly, it was observed that there were some sets of joint specimens for which the $G_{IIC}$ values after the hygrothermal aging were higher than for the respective set that was destructively tested before aging, namely for the sample sets prepared following the MO-3, RA1+FP3, R-FP-3, FC-2, and FC-3 scenarios. We attribute this finding of increased fracture toughness after hygrothermal aging to a plasticization caused by the swelling of the adhesive layer and the CFRP matrix due to a specific water uptake. Additionally, that the Skydrol contained in the R-FP series is known to react with the water from the environmental chamber, producing phosphoric acid [36]. Discriminating between such effects or deriving more detailed

insights into effects caused by reversible water uptake, e.g. a plasticization of polymeric material, or by irreversible chemical reactions with moisture, e.g. the hydrolysis of phosphoric acid esters, might be possible if re-dried aged specimens were investigated in addition to unaged and aged specimens.

### 2.6.4 Tensile Testing

In this section we present and discuss the load–displacement curves and the respective fracture patterns observed when performing a tensile testing of adhesive joints prepared from scarfed CFRP adherends. The results obtained for specimens prepared following the reference scenario or by implementing distinct scenarios characterized by introducing contaminations during the manufacturing process are presented in Fig. 2.38. In all the contamination cases, one of the adherends was contaminated while the other was intentionally left in the respective reference state, a setup intended to replicate the real-life application of repair patches.

During tensile testing, it was observed that prior to the final failure (i.e. the separation of the two adherends), all specimens presented an initial failure revealed by a first load drop in the region of the load–displacement curves, which corresponds to plastic deformation. This failure was localized at the edges of the scarfed area and is attributed to stress concentrations at this point as well as to edge effects. Having overcome this marginal fracture, the initial failure propagated along the scarfed area and led to the final separation of the two adherends.

For the specimens prepared following one of the contamination scenarios, we observed that all samples of the II-R-REF+TD1 scenario presented a higher failure

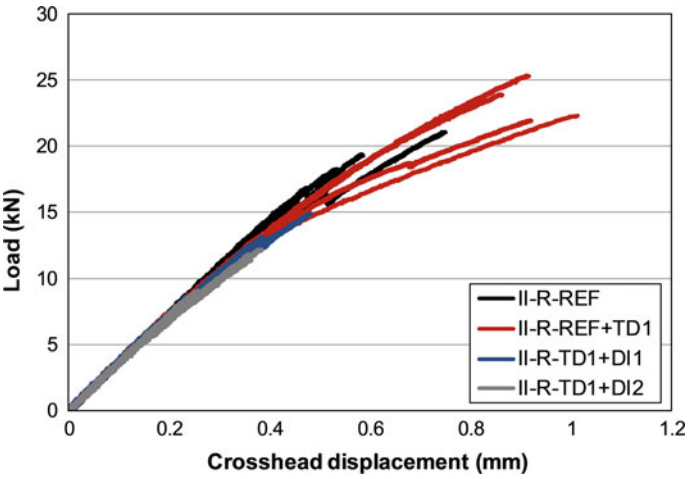


**Fig. 2.38** Load–displacement curves for adhesive joints manufactured from scarfed CFRP adherends that were prepared following the reference and contamination scenarios

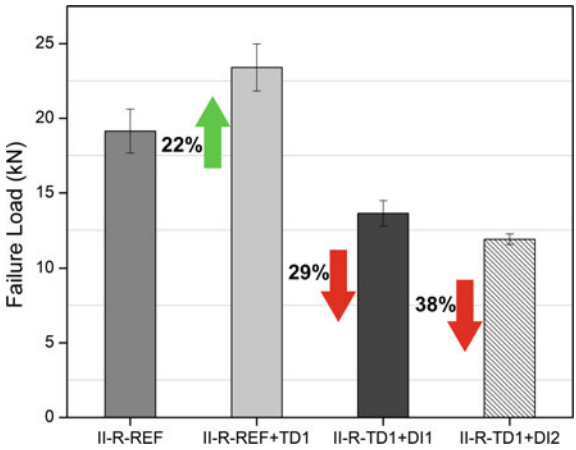


**Fig. 2.39** Failure load comparison for the scarfed samples

load, by 22%, than the reference samples (Fig. 2.39). Although the exposure of flat CFRP adherends to an elevated temperature following the TD-1 scenario decreased the fracture toughness tested in mode-I and mode-II loading, such a decrease was not prominently observed in the tensile testing of the joints prepared from scarfed CFRP adherends. Even though heat usually damages the CFRP structure or causes chemical changes in the matrix, there have been reports that high temperatures can cause oxidation of the resin which may improve adhesion due to the formation of carbonyl groups at the surface [17, 26, 27].

When implementing scenarios comprising the successive application of two contamination cases, the obtained results revealed that the contamination combining thermal impact and deposits of dried de-icing fluid had a negative effect on the mechanical performance of the scarfed repair joints, reducing the failure load as compared to specimens prepared following the reference scenario. Specifically, for samples from the TD1+DI1 scenario, the reduction of the failure load was 29%, while for the TD1+DI2 scenario the reduction reached 38% (Fig. 2.39).

Additionally, the failure surfaces of the joints were examined after the tensile tests in order to characterize the failure modes and correlate them with the tensile test results. Figure 2.40 depicts the representative fracture surfaces of each contamination scenario studied, showing the main failure modes observed in the tensile specimens.

The percentages of the different failure modes are compared for the different sample sets in Fig. 2.41. For the reference samples, a mixed-mode failure was observed, with the dominant failure being the FT failure, at 63% of the surface area, while adhesive (ADH) failure was observed for 37% of the surface area. In contrast, the tested samples prepared following the II-R-REF+TD1 case presented a higher amount of CO failure (30%), while FT failure and the ADH failure modes showed a reduction (43 and 27%) as compared to the reference samples. This change of the fracture pattern coincides with the increase in the failure load observed for the specimens prepared from scarfed adherends that had been exposed to elevated

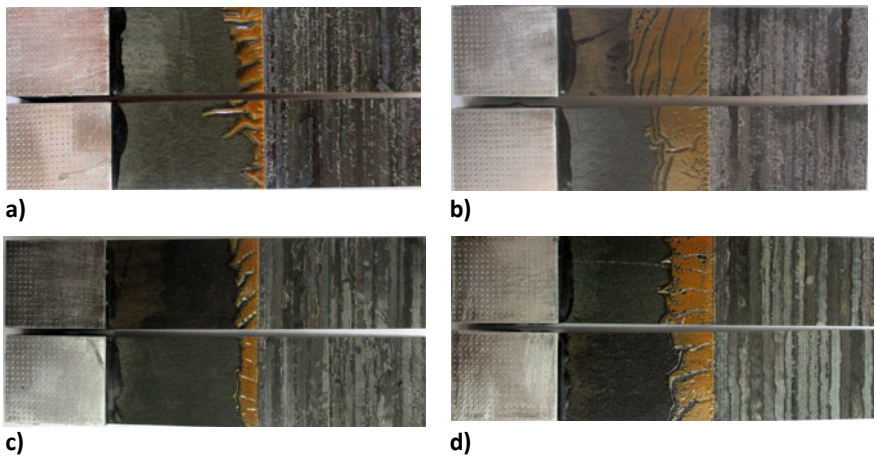


**Fig. 2.40** Images showing the representative fracture surfaces of the joints prepared from scarfed CFRP adherends obtained after loading in tension, sorted according to the contamination scenario; **a** II-R-REF; **b** II-R-REF+TD1; **c** II-R-TD1+DI1; and **d** II-R-TD1+DI2

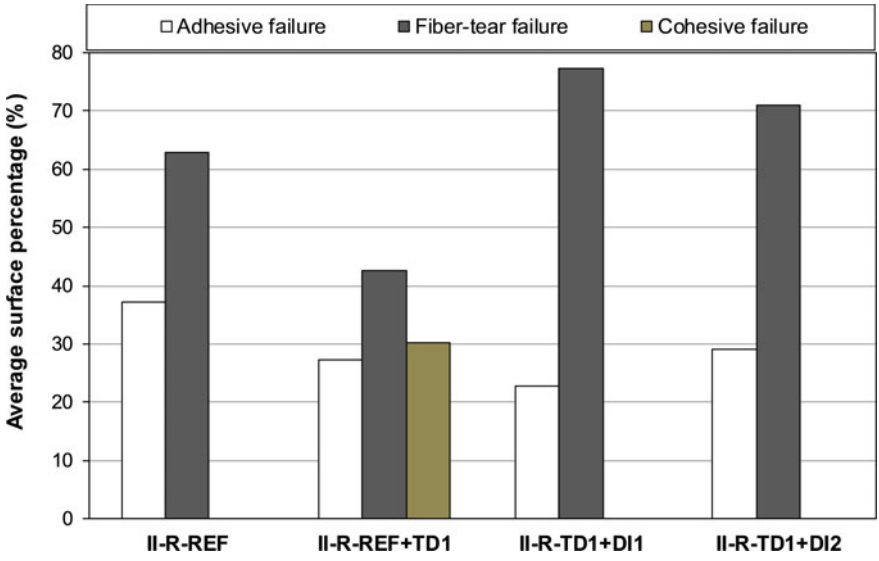


**Fig. 2.41** Average percentages of the failure modes presented in the tensile tested scarfed joints, sorted according to the contamination scenario

temperatures following the II-R-REF+TD1 scenario. When discussing these observations, the effects should be considered in relation to the loading geometry of the scarfed specimens or the performed scarfing and subsequent cleaning processes. It is plausible, according to the occurrence of a CO failure, to infer a greater amount

of energy required for a crack to develop and propagate than that required to cause an ADH or FT failure. As a consequence, an increase in the failure load is observed.

Inspecting the fracture patterns obtained for the II-R-TD1+DI1 samples, we found that the FT remained the dominant failure. The observed increase of the area percentage by 77%, as compared to samples prepared following the REF scenario, indicates that the combined successive contamination with TD1 and DI1 had a deleterious impact mainly on the behavior of CFRP adherends under tensile loading. Finally, after testing the II-R-TD1+DI2 set, the FT failure showed a slight reduction compared to the findings for II-R-TD1+DI1. Specifically, 71% of the surface area with an FT failure was observed, while ADH failure increased to 29%. These findings indicate that the TD1+DI2 combined contamination affects mainly the bondline performance (the interphase between the adherends and adhesive).

### *2.6.5 Centrifuge Test Results*

In this section, the effect of pre-bond contamination scenarios related to production and repair processes on adhesion strength between the intentionally contaminated CFRP surface and the adhesive layer is assessed based on investigations by means of the novel centrifuge testing technology. The plots shown in Fig. 2.43 and Fig. 2.45 display the average adhesion strength values, as derived from Eq. (2.5) for the applied geometry used in the tests, for the production-related and repair-related samples, respectively.

Figure 2.42 depicts representative microscope imagery revealing the different failure modes observed for the various samples. Meanwhile, Figs. 2.44 and 2.46 display the evaluated average surface area percentages of the failure modes for specimens prepared following the different production and repair-related contamination scenarios.

For all the intentionally implemented deviations from the qualified manufacture process for CFRP adherend surface preparation by applying contaminations defined for production scenarios, the results showed a decrease in the adhesion strength. This decrease was small for the low and medium contamination levels; however, for the high contamination level a more profound decrease was found. The lowest adhesion strength values were obtained for the specimens prepared following the P-MO-3 case (98% RH). The standard deviation is also considerable, but within acceptable limits for revealing the described trends. Remarkably, for all the sets of samples prepared with contaminated adherends, a significantly higher standard deviation of adhesion strength values was observed than for the P-REF specimens (Fig. 2.43).

Considering the specimens for the production-related scenarios, all the investigated fracture patterns revealed ADH and LFT failure modes (Fig. 2.44). The adhesive mainly remained on the metallic stamp, which is an indication of a stronger bond between the metallic stamp and the adhesive as compared to between the adhesive and the CFRP adherend. This stands for all cases of ADH failure here. The P-REF samples showed a much higher adhesion strength (almost double) than that of the

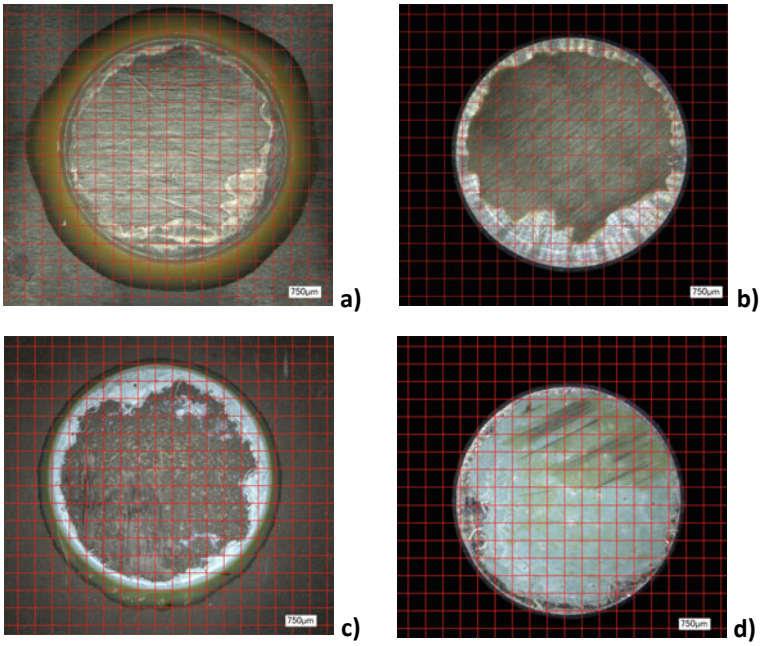


**Fig. 2.42** Representative microscopy images revealing the failure modes of centrifuge-tested CFRP samples; **a** ADH+FT for R-TD sample (CFRP side); **b** ADH+FT for R-TD sample (stamp side); **c** ADH+LFT for P-MO sample (CFRP side); and **d** ADH+LFT for P-MO sample (stamp side)

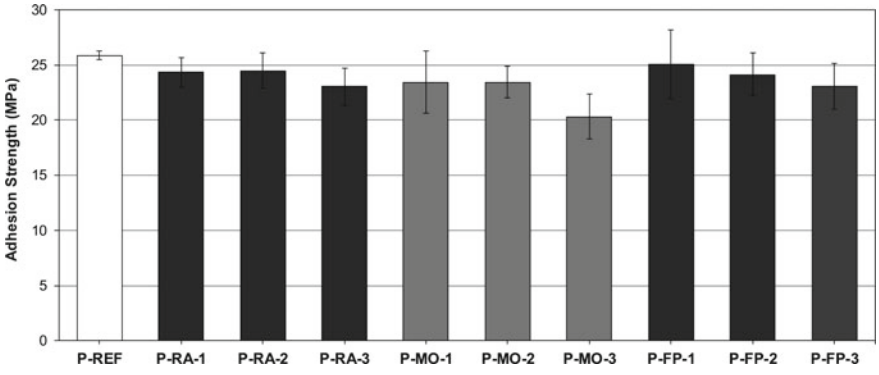


**Fig. 2.43** Adhesion strength values obtained upon centrifuge testing specimens of the production-related scenarios

R-REF samples (Fig. 2.45), which is due to the different type of adhesive used and the different curing conditions applied.

Regarding the specimen sets prepared and tested within the repair scenario, the R-REF samples (Fig. 2.45) showed a much lower adhesion strength (almost half) than

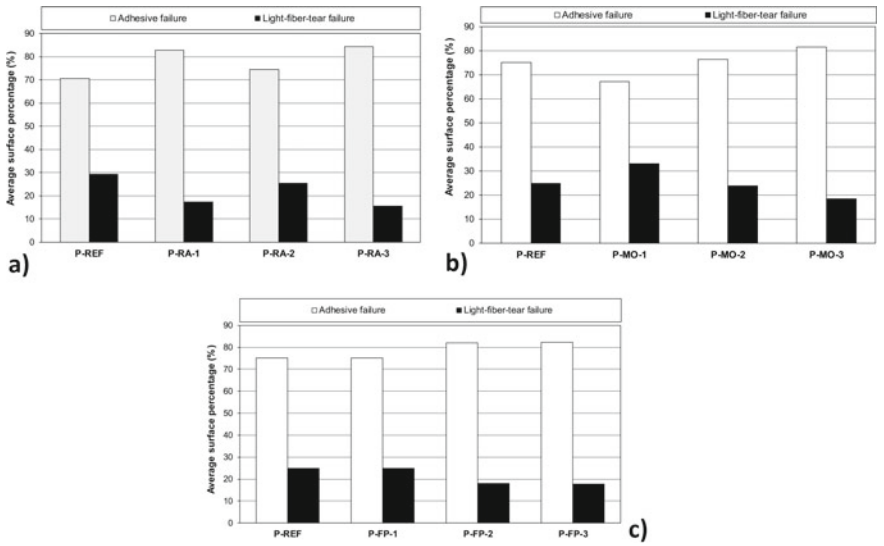


**Fig. 2.44** Average surface percentage for the different failure modes of the centrifuge-tested samples **a** P-RA, **b** P-MO, and **c** P-FP

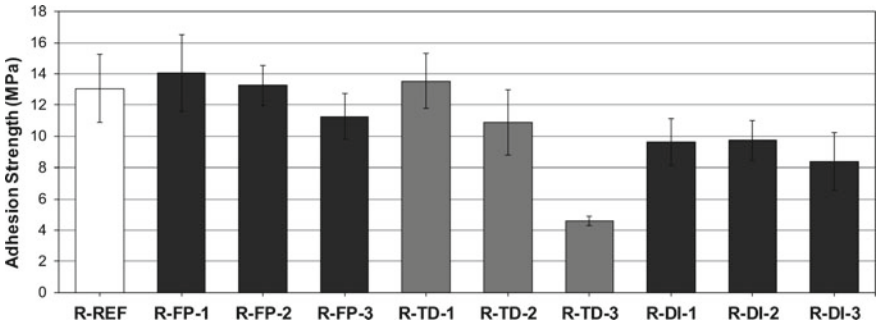


**Fig. 2.45** Adhesion strength values for the repair-related sample categories

the P-REF samples. A significantly higher relative standard deviation of the measured strength values was found for the reference scenario R-REF as compared to in the P-REF scenario. These findings are attributed to the different types of adhesive used and the different curing conditions applied.

Against the background, quite insignificant effects of the implemented deviations from the reference joining process were found. Concerning the specimens from repair-related contamination scenarios, (except for R-FP-1 and R-TD-1), a decrease of the adhesion strength was generally observed (Fig. 2.45) as compared to the specimens prepared following the R-REF scenario. For the Skydrol-based R-FP scenario, there seemed to be a slight increase in the adhesion strength for the R-FP-1

case, while an insignificant variation in the adhesion strength was observed for the R-FP-2 case and a decrease of the adhesion strength for the R-FP-3 case. However, a robust conclusion cannot be drawn for the R-FP-1 and R-FP-2 cases due to the very high standard deviation of the results for these two cases and the R-REF case. Only for the R-FP-3 case was there a considerable decrease in the adhesion strength.

The percentages of the failure modes in Fig. 2.46a reveal a similar failure behavior for the R-FP-1 case and the R-FP-2 and R-FP-3 cases, namely a decrease of the LFT failure and an increase of the ADH—which is an indication of a weak bond—and TLC failure modes.

Bearing in mind that the TD scenario mimics effects of a thermal impact on the CFRP adherends, we may assume from the finding that for specimens of the R-TD-1 case a similar behavior in terms of adhesion and failure modes is observed as for the R-REF case (Fig. 2.46b). In contrast, the R-TD-2 and R-TD-3 cases present a lower adhesion strength, and this is attributed to the degradation of the polymer matrix, which becomes effective in the first layer of the CFRP adherend because of the increased temperature, which causes the FT failure mode. The lowest adhesion strength for this set of scenarios was measured for the R-TD-3 case (corresponding to one of the CFRP adherends experiencing a pre-bond exposure of 280 °C).

Finally, for the R-DI scenario, a detrimental effect of the presence of dried de-icer was revealed for the adhesion strength of the joint. The failure mode percentages (Fig. 2.46c) show that an increase in the DI concentration causes an increase of the ADH failure mode, as the deposition of a thin layer by the de-icer acts as a barrier during the bonding of the adhesive and the CFRP adherend. However, in contrast to

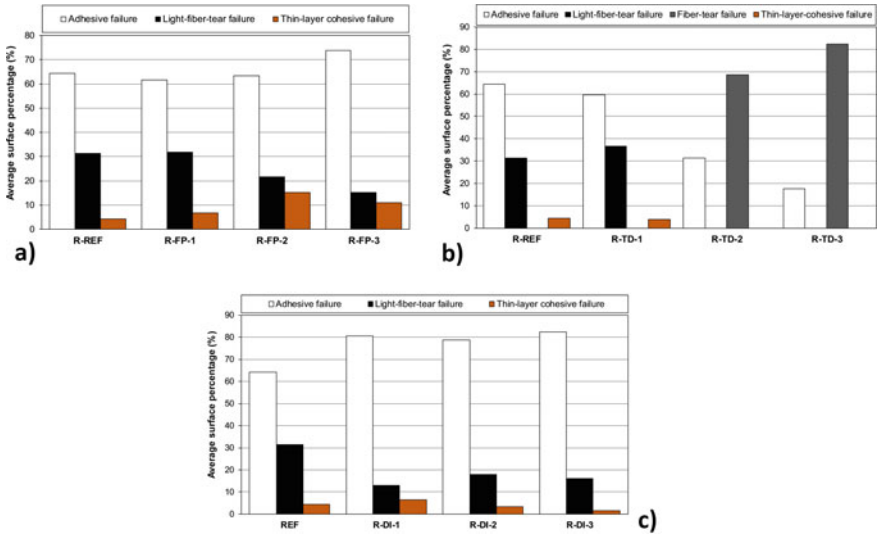


**Fig. 2.46** Average surface percentages of the different failure modes for the **a** R-FP **b** R-TD and **c** R-DI centrifuge samples

the adhesion strength, there is not a clear differentiation regarding the failure mode percentages between the different concentrations of the dried de-icer.

## 2.7 Numerical Simulation

### *2.7.1 FE Model*

A composite panel, stiffened with two stringers, was simulated under compression using the LS-DYNA FE platform. Besides the reference panel, all contamination scenarios were simulated, and their maximum load-bearing capacity was compared to the reference panel. Debonding growth was simulated using the cohesive zone model (CZM) method. This method has been widely used in the last decade to simulate the delamination progression in composite materials and the debonding progression in bonded joints, mainly due to its ease of use as it has been implemented in many commercial FE codes.

For the analysis, the linear elastic/linear softening (bilinear) traction-separation law was adopted. The constitutive law described in Fig. 2.47a is for the tension loading and separation of the adherends in the normal direction (mode-I). The mixed-mode behavior is described by the mixed-mode bilinear traction shown in Fig. 2.47b. The first region (until point 1) corresponds to the elastic part of the material's response. In this region, the material remains undamaged and the unloading at point 1 follows the elastic line. The region from point 1 to point 2 represents the material softening (damage growth) area. Once the loading has progressed beyond point 2, the material has suffered some damage (damage parameter is greater than zero but less than one), however, there is no adherend separation yet. This occurs at point 2, where the adherends separate permanently (damage parameter has reached unity). The total area under the triangle represents the energy required to debond the adherends and is known as the fracture energy. In LS-DYNA, the fracture energy

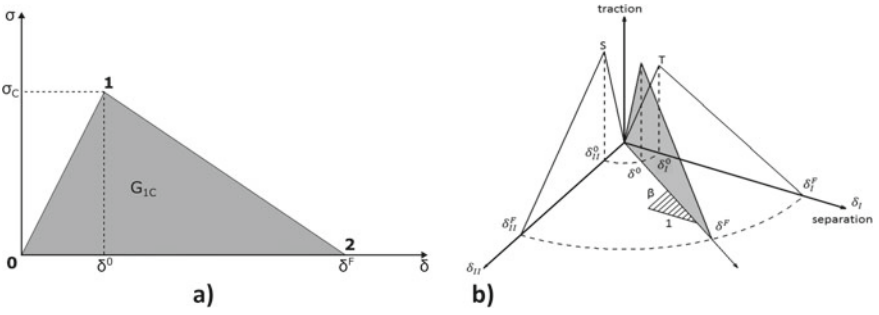


**Fig. 2.47** Schematic representation of **a** the bilinear traction-separation law for the mode-I load case and **b** the bilinear traction-separation law for the mixed-mode load case [37]

is an input parameter. It has units of energy/area. In addition, the elastic stiffness (slope) and the peak stress (point 1) are required to completely define the bilinear law.

The progressive damage modeling method was adopted to simulate the damage in the composite adherends. To this end, the material model MAT_162 of the LS-DYNA was used, which has the capacity to predict several modes of damage to the composite material. The specific material model automatically implements the progressive damage modeling method by combining a set of strain-based Hashin-type failure criteria for predicting several failure modes like tension/shear fiber failure, compression fiber failure, perpendicular matrix failure, and delamination [38].

To this end, skin, cap, and web components were modeled using standard eight-node solid elements with three degrees of freedom per node (ELFORM = 1) and MAT_162_COMPOSITE_MSC_ DMG. In addition, MAT_162 automatically applied a property degradation module to simulate the damage effects.

FE mesh was created using ANSYS Workbench and imported into the LS-DYNA FE platform. All analyses were performed using LS-DYNA. The imported mesh is depicted in Fig. 2.48.

The adhesive layer was modeled using eight-node cohesive elements with three degrees of freedom per node (ELFORM = 19) and MAT_138_COHESIVE_MIXED_MODE, which applied a mixed-mode CZM with bilinear traction-separation law to the cohesive elements. Furthermore, the debonding growth was predicted using the B-K power law.

The FE model was loaded in compression by applying displacement and the nodes were fully supported at the end of panel, as can be seen in Fig. 2.48. In addition, in order to reduce the extensive out-of-plane deformation that would cause a buckling to the panel, the nodes that are depicted in Fig. 2.48 were also supported. These nodes represent a possible anti-buckling device that could be used during mechanical tests.

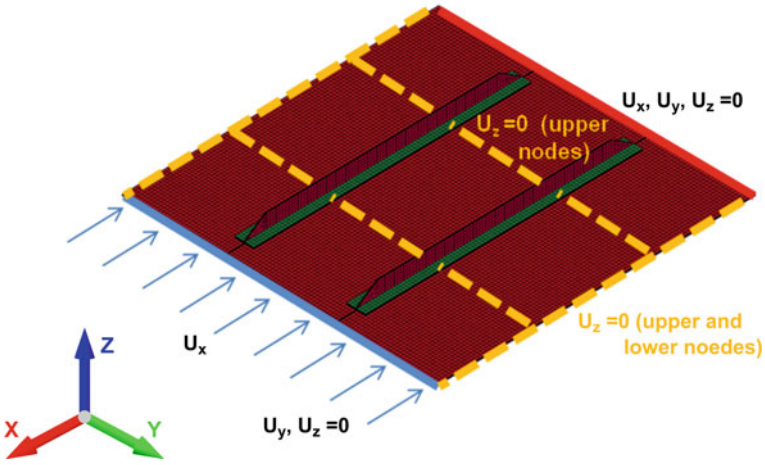


**Fig. 2.48** Applied compression and boundary conditions on a flat stiffened panel

### 2.7.2 Numerical Results

The resulting load–displacement curves for all contamination scenarios are depicted in Fig. 2.49.

The comparison concerning the maximum load for all contamination scenarios is presented in Fig. 2.50, wherein it can be observed that all contamination scenarios have a negative influence on the load-bearing capacity of the stiffened panel.

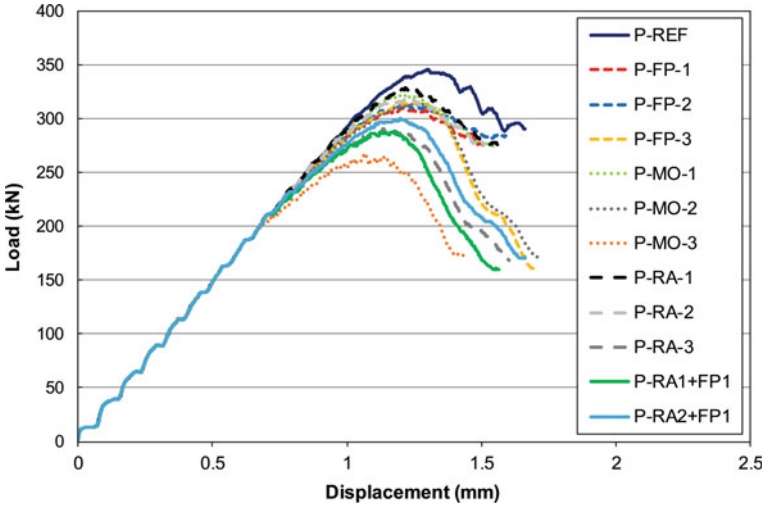


**Fig. 2.49** Load–displacement curves under compression for all contamination scenarios

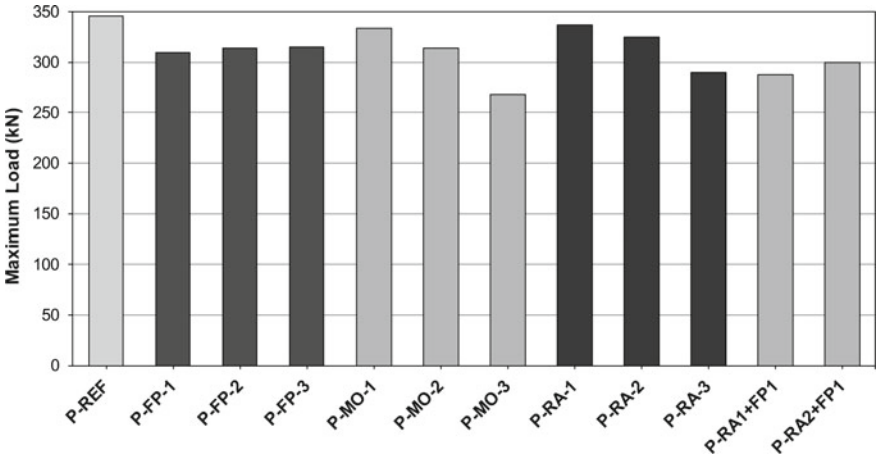


**Fig. 2.50** Predicted maximum compressive load for all contamination scenarios

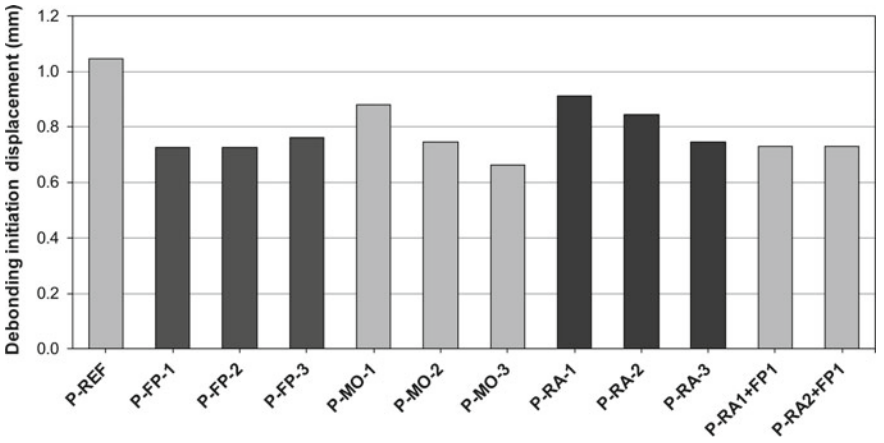


**Fig. 2.51** Predicted debonding initiation for all contamination scenarios

In Fig. 2.51, the debonding initiation displacement is presented and compared for all contamination scenarios. It is clear that all contamination scenarios have a negative impact on debonding initiation, as in all scenarios the debonding initiates earlier than in the reference case.

## 2.8 Conclusions/Synopsis

With our objective in mind of providing the reader with a feasible concept for quality assessment in adhesive bonding technology that complies with the ten heuristics and systematics described in Chap. 1, in this chapter we detail procedures to introduce disturbances from one or even several operator-related process features in scheduled ways and to test quantitative and design-relevant joint features by applying pre-process or post-process methodologies. Hereby, the exemplification is based on identifying, defining, and intentionally implementing pre-bond contamination on carbon fiber reinforced plastic (CFRP) adherends in gradational levels quantified with spectroscopic laboratory methods and identified with respect to a reference state given by the respective qualified bonding process.

The contaminants investigated within this project have a high relevance for the majority of aerospace applications. The test scenarios cover two fields of application for the adhesive bonding of primary structures, namely aircraft manufacture and in-service bonded repair. The identification of all feasible (or, pragmatically, all imaginable) disturbances of process features resulted in the definition of production and repair scenarios, yielding distinct reference surface states differing in the depth of abrasion accomplished by the CFRP grinding process. For the relevant adherends, three sample geometries were defined, namely smooth coupon samples, scarfed samples, and curved panels. The production-related disturbances comprised

the impact of release agent, moisture, or saliferous fingerprints and, with respect to repair-related disturbances, thermal impact, dried de-icing fluid, or a fingerprint with hydraulic fluid on the adherend surface; a faulty curing of the adhesive was also considered. For each of these identified and technologically crucial scenarios, we implemented discrete levels differing in the dimension of the applied contamination. Moreover, we accounted for the effects of hygrothermal aging before determining the joint strength using mode-I or mode-II testing of the fracture toughness as well as through a novel centrifuge test. In particular, specifications defined by the users of CFRP adhesive joints are often based on safeguarding adequate $G_{IC}$ values. Exceeding the respective standards, we show that joint quality is supportively and sensitively mirrored by mode-II testing of the fracture toughness as well as by the novel centrifuge test.

The present chapter describes in detail the manufacturing of the adherends for all the sample geometries (Aernnova Composites), the pre-bond single and multiple contamination and bonding of the samples (Fraunhofer IFAM), the characterization of the adherends and the joints using the XPS method (Fraunhofer IFAM), the ultrasound testing of the bonded samples (Airbus), the mechanical testing and the after-bond contamination of the samples (University of Patras), and finally the numerical simulation of the stiffened panels (University of Patras).

The manufacture of the CFRP adherends for the coupons, scarfed samples, and stiffened panels was performed under consideration of the specifications and surface quality requirements determined by the internal procedures of the manufacturing company and end users. In order to obtain a high level of repetitiveness and quality, the process of the sample preparation was carried out under aeronautical specifications and in a controlled environment.

Following the identification of the relevant three production-related and four repair-related contamination scenarios, for each scenario three levels of contamination concentration were applied, namely a low level, a medium level, and a high level. In addition, a combined contamination case for each process field was realized. The contamination of the adherends was realized by Fraunhofer IFAM and investigated using XPS analyses to measure the amount of contamination on the adherend surface and to determine the exact contaminant concentration. After the contamination procedure, the adherends were bonded in the autoclave.

The resulting joints manufactured from intentionally contaminated adherends were inspected using conventional NDT. The objective was to make a statement on the sample quality as well as on the weak bond status. All the samples were investigated using two different probes (5 and 10 MHz). For the contaminated coupons and the multi-contaminated flat samples, three different kinds of defects were observed:

1. Manufacturing defects with a marginal impact on the use of the sample for ENDT evaluation, e.g. bending of the bonded specimens, adherend surface quality issues.

2. Minor deviation from the ultrasound reference signal in the case of moist CFRP samples or sample surfaces contaminated by fingerprints (including multi-contaminated specimens). This effect could be due to contamination if only compared to the reference signal, but no further proof has been found so far.
3. Contamination-induced defects such as disbonding (faulty curing) or delamination (thermal degradation). They might have a detrimental effect on future ENDT measurements.

Conjointly with the mechanical testing results, the status of weak bonds could then be confirmed for most of the samples. Finally, curved samples were successfully tested thanks to SAUL (surface adaptive ultrasonic laws) configurations. The inspection results revealed a very low-quality sample material, probably due to the CFRP composite adherend itself. Results obtained from such samples should be evaluated and interpreted carefully.

In order to evaluate the influence of the surface state (clean, single, or multiple contaminations) of one adherend on the mechanical properties on adhesively bonded joints, established mechanical tests like mode-I and mode-II fracture toughness tests as well as tensile and centrifuge tests were conducted by the University of Patras. Mechanical testing demonstrates the contamination level that affects the mechanical strength of a bond; the results can be correlated with the results from the reference analysis methods and ENDT methods.

We shortly highlight that for each of the investigated disturbances we found significant effects on the resulting CFRP composite joint strength for at least one level of contamination applied during the bonding process. Moreover, in many cases, the lowest applied level only caused a decrease in the joint strength as compared to production or repair procedures performed following the respectively qualified process. In this way, the prepared sets of specimens encompass two challenges for the aspired process monitoring procedures: On the one hand, (the effects of) the contaminations will need to be detected, and on the other hand, the measured values will need to facilitate the discrimination between more and less relevant levels of contamination.

Specifically, the reference category exhibited the highest fracture toughness values, while for almost all cases, except from R-FP-3, the presence of the contaminant proved to be detrimental for the fracture toughness of the joints. The higher the contamination level, the higher the decrease of the joints' performance. A combined contamination results in a reduction of the fracture toughness of the bonded jointed that is greater than the reduction caused by each contaminant separately, indicating that a combination of contaminations may be more detrimental to the composite bonded joints' performance.

Additionally, a novel test was used that is both time and cost-efficient, namely the centrifuge test, whereby the adhesion strengths of all the bonded joints were measured. Besides the rather large scatter presented in some scenarios, in almost all contamination scenarios, except for R-FP-1 and R-TD-1, there was a decrease of the adhesion strength. By evaluating the centrifuge test's experimental process and results, it can be concluded that the centrifuge testing technology has great potential

to be established as a test method for the characterization of bonded joints as it is a fast testing process that generates repeatable tests capable of describing the strength of the joints.

In order to evaluate the combined effect of the pre-bond contamination and after-bond exposure to hygrothermal environment on the mode-II fracture toughness of CFRP bonded joints, the contaminated samples underwent aging inside an environmental chamber. Mostly, there was a negative effect of the contamination. After-bond hygrothermal aging significantly degrades the mode-II fracture toughness of the composite bonded joints. The decrease is larger for the contaminated samples, which reveals that the combined effect is more severe than that of the two effects separately.

Furthermore, the results of the tensile mechanical testing performed by the University of Patras revealed the effect of each contamination scenario in the tensile performance of the scarfed samples. A single contamination of an adherend with TD-1 proved to be beneficial since the sample presented a higher failure load than the reference samples. This was attributed to the enhancement of the matrix properties due to its oxidation and the formation of carbonyl groups at the surface. However, the negative effect of the combined contamination was also demonstrated. The results showed that a combined contamination of thermal degradation and de-icing fluid has a negative effect on the mechanical performance of the scarfed repair joints, reducing the failure load by up to 38%.

In total, 378 test coupons were tested using mode-I and mode-II fracture toughness tests, while 136 samples were tested using a centrifuge and tensile tests, resulting in a total of 514 tested specimens.

Finally, regarding the numerical simulations, a composite panel stiffened with two T-stringers was simulated under compression using the LS-DYNA FE platform. The comparison concerning the maximum load for the contamination scenarios showed that all contamination scenarios had a negative influence on the load-bearing capacity of the stiffened panel. Also, as a result of the contamination, the debonding initiated earlier than in the reference case.

Based on the findings achieved here, in-process ENDT will be implemented to assess features characteristic either to the pre-bond adherend surfaces (see Chap. 3) or to the adhesive joints (see Chap. 4) that were manufactured following the described intentionally applied contamination scenarios.

## References

1. Markatos DN, Tserpes KI, Rau E et al (2014) Degradation of mode-I fracture toughness of CFRP bonded joints due to release agent and moisture pre-bond contamination. J Adhes 90(2):156–173. https://doi.org/10.1080/00218464.2013.770720
2. da Silva LFM, Öchsner A, Adams RD (2011) Introduction to adhesive bonding technology. In: da Silva LFM, Öchsner A, Adams RD (eds) Handbook of adhesion technology, vol 2. Springer Berlin Heidelberg, Berlin, Heidelberg, pp 2–3

3. Charalambides MN, Hardouin R, Kinloch AJ et al (1998) Adhesively-bonded repairs to fibre-composite materials I. Experimental. Compos Part A: Appl Sci Manuf 29(11):1371–1381. https://doi.org/10.1016/s1359-835x(98)00060-8
4. Pantelakis S, Tserpes KI (2014) Adhesive bonding of composite aircraft structures: challenges and recent developments. Sci China Phys Mech Astron 57(1):2–11. https://doi.org/10.1007/s11433-013-5274-3
5. ComBoNDT "Quality assurance concepts for adhesive bonding of aircraft composite structures by advanced NDT" (2015–2018) Project funded from the European Union's Horizon 2020 research and innovation programme under grant agreement No 636494
6. Tornow C, Schlag M, Lima LCM et al (2015) Quality assurance concepts for adhesive bonding of composite aircraft structures—characterisation of adherent surfaces by extended NDT. J Adhes Sci Technol 29(21):2281–2294. https://doi.org/10.1080/01694243.2015.1055062
7. Markatos DN, Tserpes KI, Rau E et al (2013) The effects of manufacturing-induced and in-service related bonding quality reduction on the mode-I fracture toughness of composite bonded joints for aeronautical use. Compos B Eng 45(1):556–564. https://doi.org/10.1016/j.compositesb.2012.05.052
8. ENCOMB "Extended Non-Destructive Testing of Composite Bonds" (2010–2014) Project funded from the European Union's Seventh Framework Programme under grant agreement No 266226
9. AITM 1-0053—Airbus Industry Test Method (2006) Carbon fibre reinforced plastics, determination of fracture toughness energy of bonded joints, Mode I (AITM 1-0053)
10. Ebnesajjad S (2008) Adhesives technology handbook, 2nd edn. William Andrew Inc., Norwich, NY
11. Pearson RA, Blackman BRK, Campilho RDSG et al (2012) Quasi-static fracture tests. In: da Silva LFM, Dillard DA, Blackman B et al (eds) Testing adhesive joints: best practices, A221. Wiley-VCH Verlag GmbH & Co, KGaA, Weinheim, Germany, pp 163–191
12. ISO 9022-12 (2015) Optics and photonics—environmental test methods—Part 12: Contamination 37.020 (ISO 9022-12:2015)
13. Budhe S, Banea MD, Barros Sd et al (2017) An updated review of adhesively bonded joints in composite materials. Int J Adhes Adhes 72:30–42. https://doi.org/10.1016/j.ijadhadh.2016.10.010
14. Creemers F, Geurts KJ, Noeske M (2016) Influence of surface contaminations on the quality and bond strength of structural adhesive joints. In: European adhesion (EURADH) conference
15. Gause RL (1989) A noncontacting scanning photoelectron emission technique for bonding surface cleanliness inspection (NASA TM-100361 Technical Memorandum)
16. Moutsompegka E, Tserpes KI, Polydoropoulou P et al (2017) Experimental study of the effect of pre-bond contamination with de-icing fluid and ageing on the fracture toughness of composite bonded joints. Fatigue Fract Eng Mater Struct 40(10):1581–1591. https://doi.org/10.1111/ffe.12660
17. Tserpes KI, Markatos DN, Brune K et al (2014) A detailed experimental study of the effects of pre-bond contamination with a hydraulic fluid, thermal degradation, and poor curing on fracture toughness of composite-bonded joints. J Adhes Sci Technol 28(18):1865–1880. https://doi.org/10.1080/01694243.2014.925387
18. Hollander JM, Jolly WL (1970) X-ray photoelectron spectroscopy. Acc Chem Res 3(6):193–200. https://doi.org/10.1021/ar50030a003
19. ASTM International D5573-99 (2005) Standard practice for classifying failure modes in fiber-reinforced-plastic (FRP) Joints 83.120 (ASTM D5573-99). www.astm.org
20. AITM 1-0006—Airbus Industry Test Method (1994) Carbon fibre reinforced plastics, determination of interlaminar fracture toughness energy—Mode II (AITM 1-0006)
21. Hoffmann M, Tserpes K, Moutsompegka E et al (2018) Determination of adhesion strength of pre-bond contaminated composite-to-metal bonded joints by centrifuge tests. Compos B Eng 147:114–121. https://doi.org/10.1016/j.compositesb.2018.04.014
22. Rietz U, Lerche D, Hielscher S et al (2015) Centrifugal adhesion testing technology (CATT)—a valuable tool for strength determination. J Adhes Soc Jpn 51(s1):293–297. https://doi.org/10.11618/adhesion.51.293

23. LUM GmbH (2018) Technical specification od Adhesion Analyser LUMiFrac. https://www.lum-gmbh.com. Accessed 25 June 2018
24. Beck U, Reiners G, Lerche D et al (2011) Quantitative adhesion testing of optical coatings by means of centrifuge technology. Surf Coat Technol 205:S182–S186. https://doi.org/10.1016/j.surfcoat.2011.02.016
25. DIN EN 2823 European Association of Aerospace Industries (1998) Aerospace series—fibre reinforced plastics—determination of the effect of exposure to humid atmosphere on physical and mechanical characteristics (DIN EN 2823)
26. Choi DM, Park CK, Cho K et al (1997) Adhesion improvement of epoxy resin/polyethylene joints by plasma treatment of polyethylene. Polymer 38(25):6243–6249. https://doi.org/10.1016/S0032-3861(97)00175-4
27. Ochoa-Putman C, Vaidya UK (2011) Mechanisms of interfacial adhesion in metal–polymer composites—effect of chemical treatment. Compos A Appl Sci Manuf 42(8):906–915. https://doi.org/10.1016/j.compositesa.2011.03.019
28. Cysne Barbosa AP, Fulco PAP, Guerra ESS et al (2017) Accelerated aging effects on carbon fiber/epoxy composites. Compos B Eng 110:298–306. https://doi.org/10.1016/j.compositesb.2016.11.004
29. Collins DH, Freels JK, Huzurbazar AV et al (2013) Accelerated test methods for reliability prediction. J Qual Technol 45(3):244–259. https://doi.org/10.1080/00224065.2013.11917936
30. Ewert U, Jaenisch GJ, Osterloh K et al (2011) Performance control: nondestructive testing and reliability evaluation. In: Czichos H, Saito T, Smith L (eds) Springer handbook of metrology and testing. Springer, Berlin, Heidelberg
31. Johnson WS, Butkus LM (1998) Considering environmental conditions in the design of bonded structures: a fracture toughness mechanics approach. Fatigue Fract Eng Mater Struct 21(4):465–478. https://doi.org/10.1046/j.1460-2695.1998.00533.x
32. Liljedahl CDM, Crocombe AD, Wahab MA et al (2007) Modelling the environmental degradation of adhesively bonded aluminium and composite joints using a CZM approach. Int J Adhes Adhes 27(6):505–518. https://doi.org/10.1016/j.ijadhadh.2006.09.015
33. Pitt S, Jones R, Peng D (2012) Characterization of the durability of adhesive bonds. Fatigue Fract Eng Mater Struct 35(11):998–1006. https://doi.org/10.1111/j.1460-2695.2012.01688.x
34. Mubashar A, Ashcroft IA, Critchlow GW et al (2011) A Method of predicting the stresses in adhesive joints after cyclic moisture conditioning. J Adhes 87(9):1061–1089. https://doi.org/10.1080/00218464.2011.600675
35. Bowditch MR (1996) The durability of adhesive joints in the presence of water. Int J Adhes Adhes 16(2):73–79. https://doi.org/10.1016/0143-7496(96)00001-2
36. Moutsompegka E, Tserpes KI, Brune K et al (2017) The effect of pre-bond contamination with fingerprint and ageing on the fracture toughness of composite bonded joints. In: 7th EASN international conference on innovation in European aeronautics research, 26–29 September, Warsaw, Poland
37. Floros IS, Tserpes KI, Löbel T (2015) Mode-I, mode-II and mixed-mode I+II fracture behavior of composite bonded joints: experimental characterization and numerical simulation. Compos B Eng 78:459–468. https://doi.org/10.1016/j.compositesb.2015.04.006
38. Tserpes KI, Peikert G, Floros IS (2016) Crack stopping in composite adhesively bonded joints through corrugation. Theoret Appl Fract Mech 83:152–157. https://doi.org/10.1016/j.tafmec.2015.10.003